

Part-scale Thermal Simulation of Laser Powder Bed Fusion Using Graph Theory:  
Effect of Thermal History on Porosity, Microstructure Evolution, and Recoater Crash

Reza Yavari<sup>1\*</sup>, Ziyad Smoqi<sup>1</sup>, Alex Riensche<sup>1</sup>, Ben Bevans<sup>1</sup>, Humaun Kobir<sup>1</sup>, Heimdall  
Mendoza<sup>2</sup>, Hyeyun Song<sup>2</sup>, Kevin Cole<sup>1</sup>, Prahalada Rao<sup>1</sup>

<sup>1</sup>Mechanical and Materials Engineering, University of Nebraska-Lincoln, Lincoln, NE, USA

<sup>2</sup>Additive Manufacturing, Edison Welding Institute, Columbus, OH, USA

**Abstract**

Flaw formation in laser powder bed fusion (LPBF) is influenced by the spatiotemporal temperature distribution – thermal history – of the part during the process. To prevent flaw formation there is a need for fast and accurate models that can predict the thermal history as a function of the part shape and processing parameters. In previous work, a thermal modeling approach based on graph theory was used to predict the thermal history in LPBF parts in less-than 20% of the time required by finite element-based models with error within 10% of experimental measurements. The present work transitions toward the use of the graph theory approach for predicting flaw formation. The objectives of this paper are: (1) to apply the graph theory approach for predicting the thermal history of several LPBF parts that have different geometries but were all built together on a single build plate; (2) to compare the graph theory thermal model with experimental temperature measurements made using an in-situ infrared camera; and (3) to relate the thermal history predictions obtained from the graph theory approach to flaw formation in LPBF parts. In pursuit of these objectives, fifteen different Inconel 718 parts encompassing five different shapes were built simultaneously on an open architecture LPBF platform (build time 9.5 hours). Second, the LPBF machine was instrumented with an in-situ infrared camera to capture the layer-wise surface temperature of each part as it was being deposited. Third, the thermal history for each part was predicted with the graph theory approach, and the model predictions were assessed against experimental temperature measurements. Fourth, the porosity in certain test parts was quantified with X-ray computed tomography, and their microstructure was characterized with optical and scanning electron microscopy. The results show that the shape of the part has a significant effect on the thermal history, and thereby influences the occurrence of build failures (recoater crash), type and severity of porosity, and morphology of the microstructure. The graph theory approach correctly predicts the thermal history trends that lead to flaw formation in LPBF within a fraction of the build time – the root mean squared prediction error is less-than 20 °C, and computation time is approximately 5 minutes. The graph theory method has the potential to serve LPBF practitioners as a rapid physics-based approach to guide part design and identify suitable processing parameters in place of expensive and time-consuming empirical trial-and-error optimization.

**Keywords:** Thermal Simulation; Powder Bed Fusion; Porosity; Microstructure; Recoater Crash

\*corresponding author, email: [mrezayavari89@huskers.unl.edu](mailto:mrezayavari89@huskers.unl.edu)

## 1.1 Overview

Laser powder bed fusion (LPBF) is a metal additive manufacturing process in which a layer of material in powder form is deposited on a build plate (powder bed) and selectively melted using energy from a laser [1]. As shown in Figure 1, in LPBF the powder is deposited onto the build plate using a blade (recoater) or roller-type mechanism. After a layer of powder is melted by the laser, a fresh layer of powder is deposited, and the process repeats until an entire part is built. Contemporary LPBF systems are typically equipped with a 250 W to 500 W fiber laser with an operating wavelength in the near infrared region (1050 to 1070 nm). The laser is scanned in the horizontal plane using a pair of galvanometric mirrors, with the typical scanning velocity in the range of 500 to 1000 mm·s<sup>-1</sup>.

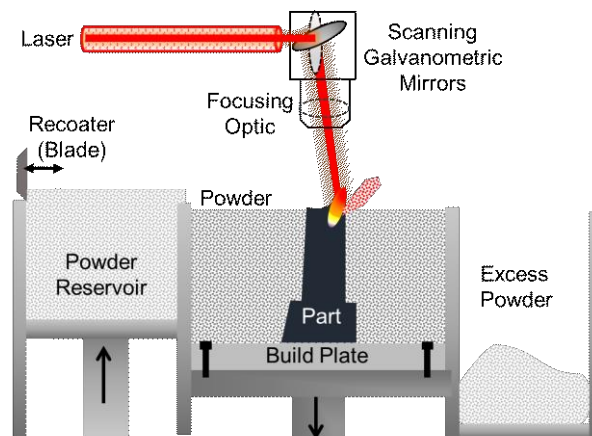


*Figure 1: A schematic of the laser powder bed fusion (LPBF) process.*

The LPBF process continues to evolve as the process of choice for creation of complex, high-value components, particularly in the aerospace, tool and die, automotive, and biomedical industries [2, 3]. For example, to make an aerospace part weighing one pound of material requires the machining of 20 pounds of raw material - a buy-to-fly ratio of 20:1 [4]. With LPBF, researchers have demonstrated that it is possible to achieve a buy-to-fly ratio as low as 7:1, resulting in considerable cost savings. Moreover, the lead time shrinks from months to weeks [3, 4].

Despite the foregoing advantages, consistency and the occurrence of flaws are major impediments in the widespread use of LPBF components in mission-critical applications [5, 6]. Exemplified in Figure 2 is a type of frequent LPBF process anomaly called recoater crash or recoater impact [7]. This particular recoater crash is caused by deformation of an arch-shaped part in the vertical build direction (Z direction) during the process [8].

In Figure 2, the deformation of the part was sufficiently large for it to protrude above the powder bed, a phenomenon termed as *superelevation* [9]. Referring to Figure 2, the two arch-shaped parts demarcated in the top left of the powder bed are superelevated. These superelevated parts came in contact with the recoater blade as a new layer of powder was being deposited, consequently, the arches were sheared. A recoater crash can also lead to material debris being dragged across the powder bed, leading to flaw formation in nearby parts on the build plate.

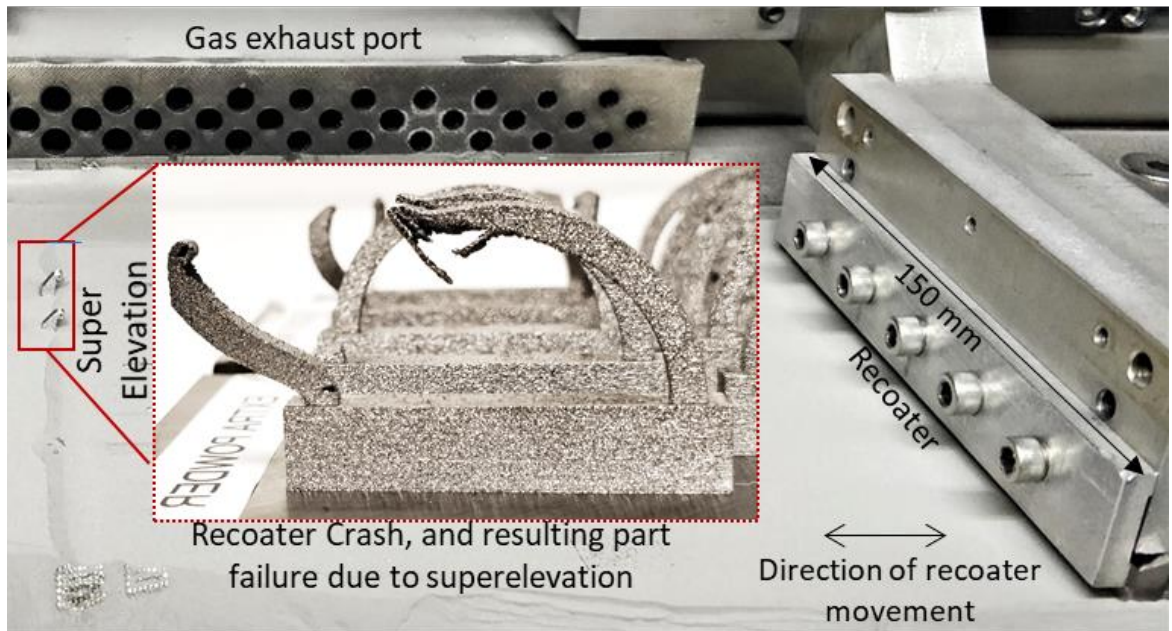


Figure 2: An example of a build failure due to superelevation of an arch-shaped part studied in this work. Thermal-induced deformation caused the part to rise above the powder bed, and subsequently, make contact with the recoater (recoater crash or impact).

## 1.2 Motivation and Challenges

Flaw formation and process failures in LPBF, such as the recoater crash described in the context of Figure 2, are governed by the magnitude, spatial distribution and temporal trends of temperature in the part as it is being printed [10]. The spatiotemporal distribution of temperature, called the thermal history, is a function of the material, part geometry (shape), and processing parameters, such as the power and scanning speed of the laser, and the part orientation [7, 11-13].

Depending on its shape and processing parameters, certain regions of the part may retain heat or cool more slowly compared to others [14, 15]. The uneven heating and cooling of the part is the root cause of flaw formation in LPBF [1]. To ensure part quality, practitioners currently resort to empirical build-and-test studies to identify the optimal LPBF processing parameters and part geometry [16]. Parameters optimized by empirical testing of simple-shaped coupons followed by data-driven process monitoring may not work for all part shapes, especially components with complex-shaped features, such as overhangs and thin-walls [17-19].

Moreover, empirical testing is expensive and cumbersome, given the large design and parameter space. Therefore, to ensure part quality in LPBF, it is imperative to augment experiments with fundamental understanding of the causal thermal phenomena at the root of flaw formation [3, 20-23]. In other words, physics-guided design and process planning is needed for LPBF [24-26].

Accordingly, fast and accurate thermal models of the LPBF process are critical in the following contexts: (a) obtaining theoretical insight into the factors driving the thermal physics of LPBF, leading to evolved understanding of the fundamental reasons for flaw formation, such as microstructural heterogeneity and part distortion, (b) optimizing the part geometry and processing parameters based on an understanding of the thermal physics, as opposed to extensive empirical

testing, and (c) estimate the thermal history in the part before it is built, and using these predictions with in-situ experimental data for early detection of process drifts [16, 24-33].

Currently thermal modeling in LPBF is largely based on finite element (FE) modeling [34-39]. One challenge stems from the prohibitive computational burden of non-proprietary FE-based thermal modeling [39-44]. Commercial FE-based solutions for thermal modeling in LPBF, such as Autodesk Netfabb and Ansys 3DSim, have reduced the computation time through adaptive meshing techniques [45, 46]. However, the algorithms are proprietary, and the model predictions have yet to be validated independently. An extant gap in the literature is to predict flaw formation and process failure as a function of the part-level temperature distribution. While commercial software can provide estimation of distortion and build failures due to recoater crash, recent benchmarking studies have found a large variation in the distortion predictions by different commercial software [45].

### **1.3 Objective and Approach**

This work concerns thermal modeling in LPBF using the concept of heat diffusion on graphs (graph theory) [47-49]. The objectives of this paper are as follows:

- (1) Apply the mesh-free graph theory approach to predict the thermal history of multiple parts built simultaneously on a LPBF system.
- (2) Verify the graph theory-derived predictions with experimental temperature measurements.
- (3) Correlate the effect of part shape on the thermal history, and part quality (microstructure evolution, porosity, and build failures).

In pursuit of these objectives, we framed the following four tasks. First, we built fifteen different parts encompassing five different geometries simultaneously on an open architecture LPBF platform at Edison Welding Institute. Second, we instrumented the LPBF machine with an

in-situ infrared thermal camera and captured the layer-wise surface temperature of each part as it was being processed. Third, we predicted the temperature distribution for each part using the graph theory approach and verified the predicted temperature trends with experimental temperature measurements obtained by the thermal camera. Fourth, to explain how and why the temperature distribution influences flaw formation, we examined the parts with X-ray computed tomography (for visualization and quantification of flaw formation), and optical and scanning electron microscopy (for characterizing the microstructure evolution).

The rest of this paper is organized as follows. In Sec. 2, we describe the experimental setup, test parts, and procedure to obtain temperature measurements. In Sec. 3, we elucidate the graph theory approach. In Sec. 4, we apply the graph theory approach to predict the thermal history in the various test parts, and correlate the temperature distribution with the porosity and microstructure evolution. Lastly, conclusions and directions for future research are summarized in Sec. 5.

## **2 Experiments**

### **2.1 Open Architecture LPBF Platform**

In this work, experiments were conducted on an open architecture LPBF platform at Edison Welding Institute, Columbus, Ohio. The schematic and pictures of the setup are shown in Figure 3. The system was integrated with a thermal camera inside the chamber to acquire the surface temperature measurements of the part as it was being built. The thermal camera was inclined at  $80^\circ$  to the horizontal. The specifications of the LPBF system and thermal camera are reported in Table 1.

The thermal camera (Micro Epsilon, model TIM 640) had a spectral range of 8 to 14  $\mu\text{m}$  (longwave infrared spectrum), and an optical resolution of 640 pixels  $\times$  480 pixels. The thermal camera was positioned at a height such that it captured an approximately 125 mm  $\times$  125 mm area

of the build plate. The spatial resolution was  $\sim 20$  pixels per  $\text{mm}^2$ . The thermal camera was triggered to capture images of the powder bed only when the laser is actively melting a layer. The thermal camera stopped recording when the laser finished scanning a layer. In other words, the camera was turned on only when the laser was active.

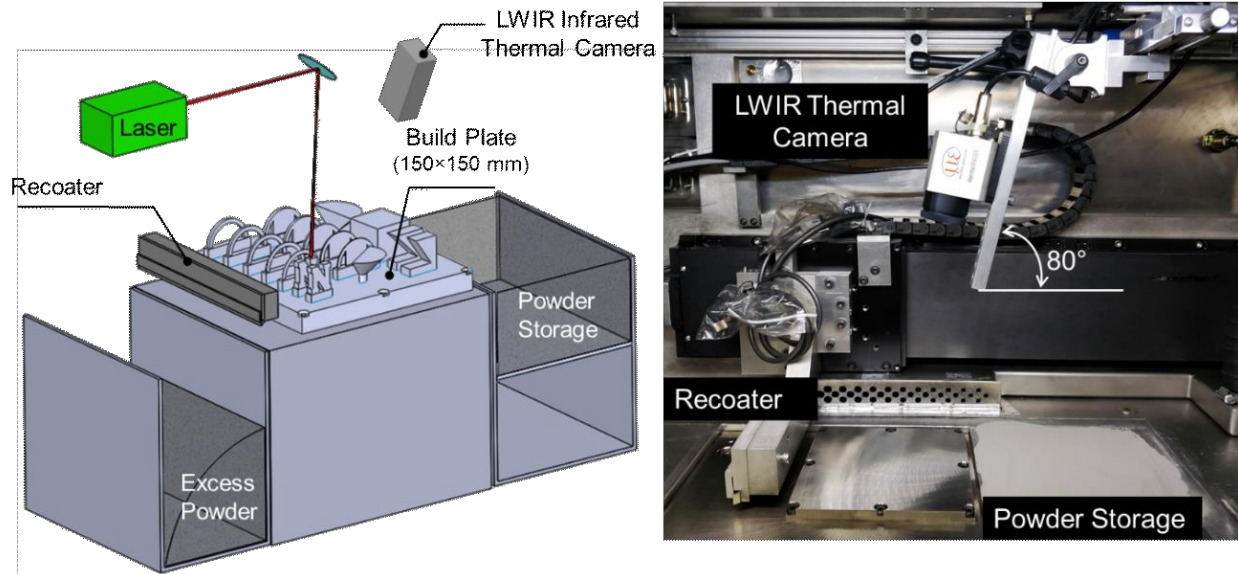


*Figure 3: The schematic and photograph of the open architecture LPBF platform. A longwave infrared thermal camera located above the build plate and inclined at  $80^\circ$  to the horizontal plane is used to capture the part surface temperature during the build process.*

Temperature measurement in LPBF is predominantly based on infrared thermography of the surface layers, as there is no practically viable approach to observe the temperature trends in the interior of an LPBF part without halting the process. For example, a thermocouple can be brazed inside the part by stopping the process. However, stopping the process will alter the thermal history and increase the time between layers, and thereby occlude the objective of correlating the temperature distribution with the microstructure and porosity formation [50].

Another alternative is to braze multiple thermocouples to the build plate [51]. Using this approach, it is possible to obtain the temperature trends for a few tens of layers before the temperature signatures are attenuated due to damping by heat conduction through increasing distance from the laser [50, 52].

*Table 1: Summary of material and process parameters.*

Process Parameter	Values [units]
Laser type and wavelength.	Ytterbium fiber, wavelength 1070 nm continuous mode (manufacturer IPG)
Laser power (P) [W]	285
Scanning Speed (V) [mm·s <sup>-1</sup> ]	960
Hatch spacing (H) [mm]	0.1
Layer thickness (T) [mm]	0.04
Stripes overlap [mm]	0.08
Stripe width [mm]	10
Volumetric global energy density [J/mm <sup>3</sup> ] $E_v = P/(H \times V \times T)$	74
Laser spot size [μm]	80
Scanning strategy	Meander-type scanning strategy with 45 degree rotation of scan path between layers.
Build atmosphere	Argon
Build plate Preheat temperature [°C]	110
Material Properties	Values [units]
Material type	Carpenter Additive CT PowderRange 718; corresponding to UNS N07718
Particle size range [mm]	0.01 – 0.04
IR Thermal Camera Specifications	Values
Brand and model	Micro Epsilon – thermoIMAGE TIM 640
Resolution [pixels]	640 × 480
Frame rate [Hz]	32
Spectral range [μm]	8 to 14
Spatial resolution of object in image	20
Camera On trigger [pixels per mm <sup>2</sup> ]	Laser on.
Image size [mm]	125 × 125

## 2.2 Build Plan

The test parts in this work were made using Carpenter Additive CT PowderRange 718 powder material, which is equivalent to Inconel 718 (UNS N07718). Seventeen parts encompassing six different types of geometries were built in total on a single build plate as shown in Figure 4. Out of these seventeen parts we selected fifteen parts having five different geometries for further study. The processing parameters selected for this work are based on prior studies with similar material, and are reported in Table 1 [53]. The salient aspects of each of the test parts is described in the context of Figure 4 and Table 2.



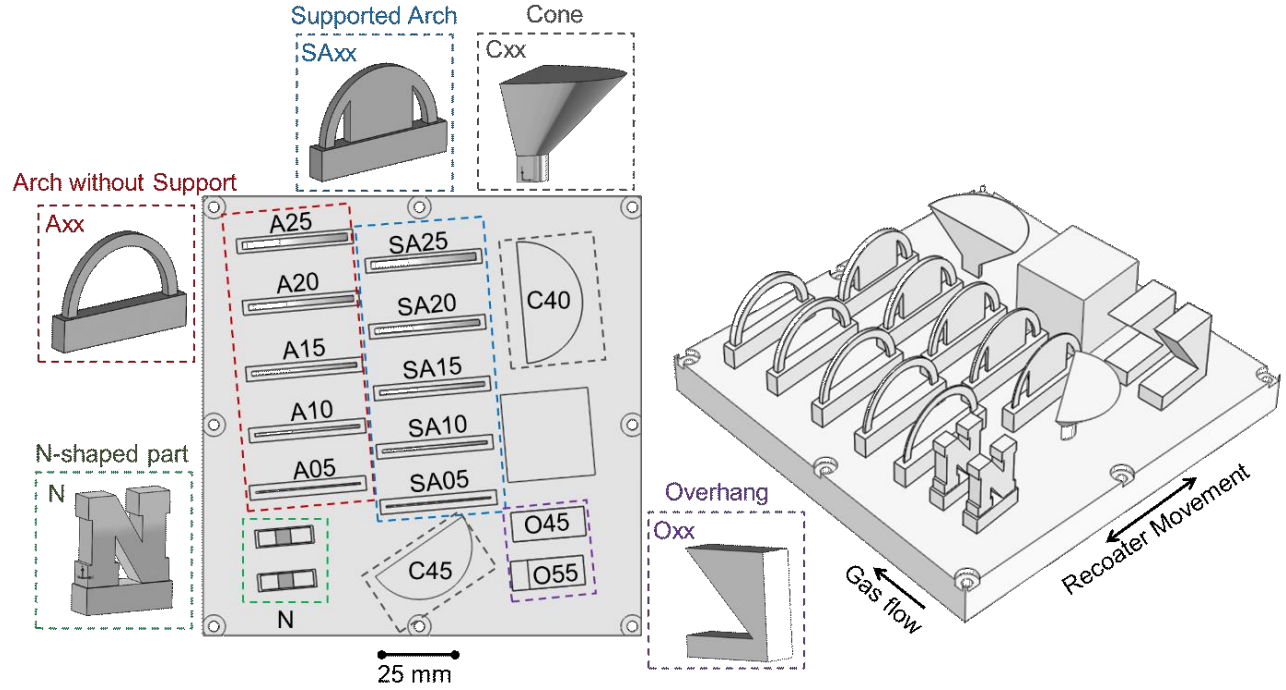
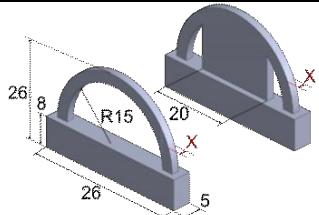
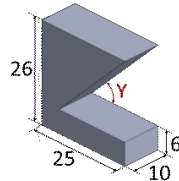
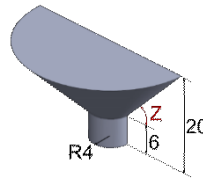
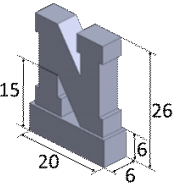


Figure 4: The top view of the build plate with the five different types of test geometries studied in this work. On the right is the isometric view of the build plate facing the front of the machine. The parts were produced using conditions reported in Table 1.

Table 2. The five test geometries studied in this work, along with the critical dimensions of the part that are varied.

	Arch	Overhang	Cone	N-shaped
Part Geometries (mm)				
Critical Dimensions	X= 0.5, 1, 1.5, 2, and 2.5 mm	Y = 45°, 55°	Z = 40°, 45°	-
Nomenclature	Arch without support A[10 × X] Supported Arch SA[10 × X]  Arch with X = 0.5 mm: A05 Supported Arch X = 1 mm: SA10	O[Y] Overhang with Y = 45°: O45 Overhang with Y = 55°: O55	C[Z] Cone with Z = 40°: C40 Cone with Z = 45°: C45	N
Post Processing	-	Porosity with X-ray computed tomography (XCT), metallography and scanning electron microscopy		-
Outcome	Predict thermal history as a function of thickness (X), Correlate thermal history with (recoater crash) with the temperature distribution	Model calibration with C45, Predict thermal history as a function of overhang angle, Correlate thermal history with porosity and microstructure evolution		Model Verification

### *2.2.1 Limitations and Mitigating Strategies*

#### **(1) Processing parameters**

We note that the thermal history, and subsequently, the quality of the LPBF part is governed by several processing parameters, such as laser power, velocity, and scanning strategies [54-58]. Investigating these effects will be part of our future endeavor. Since the objective of this work is to validate the graph theory approach with experimental data obtained from parts with differing geometries, and subsequently, correlate the predicted thermal history with microstructure evolved and process faults (recoater crash). Accordingly, the scanning strategy and process parameters were maintained constant to observe and ascertain the effect of geometry (part design) on the temperature history.

Currently, the graph theory approach is implemented in a meta-layer approach. Hatch-level scanning is not implemented in the current paper, but the possibility was noted in our previous works [48]. In the current paper, we used the stripe-based scanning strategy with the hatch spacing of 0.1 mm, stripe overlap of 0.08 mm and stripe width of 10 mm for all the geometries through all the layers.

Remelting, which refers to scanning the layers more than once has not been applied in our builds. Remelting is advantageous as it has been demonstrated to increase the density and reduce the occurrence of lack-of-fusion porosity [56]. Remelting and investigating different scanning pattern (stripes, chessboard, etc.) or different hatch spacing is a pathway for future exploration.

#### **(2) Positioning (location) and orientation of parts**

In LPBF, apart from the processing parameters, the orientation of part and its location on the build plate (layout), sequence of printing, build atmosphere, among others, influences the quality of the part [54, 59]. For example, the focal length of laser could vary from center to corner of the build plate. This change in the laser focus height can lead to part flaws.

In this work we adopted the following procedures to minimize the effect of variations in build location and part orientation.

- (a) The Open Architecture System at EWI is capable of accommodating a  $250 \times 250$  mm build plate. However, we used a build plate of only  $150 \times 150$  mm to minimize the effect aberrations in the laser focus height on parts located near the edges of the build platform.
- (b) To protect finer parts such as arches, these were placed at the far-side of the build plate from the start position of the recoater. The narrowest cross-section of the arches were inclined to the motion of the recoater to minimize shear forces on the part from the recoater motion. Similarly, all the parts are angled to the recoater to avoid large shear forces.
- (c) The arches are flanked by parts with larger thermal mass to mitigate failure. The rationale is that parts with larger thermal mass tend to distort more than parts with a smaller parts, and thus tend to lift the recoater slightly from the powder bed. The lifting of the recoater blade reduces the possibility of the recoater impacting a smaller part.
- (d) to avoid spatter and debris from one part interfering with others, the parts are spaced with at least 5 mm gaps between each other and in a staggered manner.
- (e) The parts were located to facilitate the exhaust of soot particles away from a fresh deposited layer. The gas flow in this machine was from the front to the back of the machine which is shown with arrow in Figure 4; noting that the gas exhaust port is to far-side from the door as seen in Figure 1 and Figure 3. Hence, the laser melted the parts in the reverse order of the gas flow – the laser processes the parts from back to front of the build plate. By processing parts closer to the exhaust port first minimizes the chance of soot particles interfering with parts that are yet to be melted.

### 2.2.2 Cone-shaped Parts (C40, C45)

Two cone-shaped parts of height 20 mm were produced. We varied the inclination of the slant edge of the cone to the horizontal defined as the overhang angle. We built cones with the slant edge inclined at two overhang angles, namely,  $Z = 40^\circ$  and  $Z = 45^\circ$ . The corresponding cone-shaped parts were labeled C40 and C45, respectively. A previous work reported by Hooper *et al.* [60] shows that the change in cooling rate and surface temperature as a function of the build height for such cone-shaped parts results in microstructure heterogeneity and porosity.

Furthermore, one of the cone shaped parts (C45) was used to calibrate the parameters of the graph theory model. Both the cone-shaped parts had a build height of 20 mm, compared to the rest of the parts on the build plate which had a total build height of 26 mm. We anticipated that the build failure in the arch-shaped test artifacts would occur beyond 20 mm build height. Consequently, the thermal history of the cone-shaped parts would not be affected by any build failures that were to occur beyond a 20 mm in other parts.

### 2.2.3 N-Shaped Part

The graph theory model was calibrated with the data from the cone-shaped part C45, and the accuracy of the predictions was tested in the context of data from the N-shaped part. Using the same simulation parameters to predict the thermal history of a relatively complex geometry ensures that the model is accurate, and viable for extrapolation to other geometries.

Two N-shaped parts were created in this work, one of which had a lattice-like interior structure and the other N-shaped part had a conventional fully consolidated interior. We have not analyzed the lattice-like N-shaped part.

#### 2.2.4 *Prismatic Overhang Part (O45 and O55)*

This part geometry has been studied previously in Refs. [33, 61]. We studied the effect of the overhang angle ( $Y = 45^\circ$  and  $55^\circ$ ) on the microstructural evolution and porosity through metallography and XCT, respectively. The parts were labeled O45 and O55 corresponding to the overhang angle  $Y$ . A key difference of these prismatic overhang parts compared to the cone-shaped parts is the presence of a base with a large width and cross-sectional area, which facilitates the conduction of heat to the base plate. In contrast, the cone-shaped parts had a narrow cylindrical base. Consequently, the temperature gradients in O45 and O55 were expected to be less prominent compared to the cone-shaped parts.

#### 2.2.5 *Arches with and without supports*

Two types of arch-shaped parts were built with and without supports, prefixed with the label SA and A, respectively. These arch-shaped parts enabled the study of three design-related aspects on the thermal history: (i) the effect of the cross section or thickness of the arch, (ii) overhang angle, and (iii) presence of supports [62].

Referring to Figure 4, the feature controlled in these arches is the thickness, marked with the dimension  $X$ . The values of  $X$  were varied at five levels, namely, 0.5 mm, 1 mm, 1.5 mm, 2 mm, and 2.5 mm. The corresponding arches without support were labeled A05, A10, A15, A20, and A25. Similarly, the arches with support were labelled SA05 for  $X = 0.5$  mm, SA10 for  $X = 1$  mm, and so on.

The angle of inclination of the arch to the horizontal (overhang angle,  $X$ ) changes with the build height. The overhang angle of the arch was  $90^\circ$  at its start at layer 200 and reduced to  $0^\circ$  on completion at layer 650. In other words, at layer 650 the overhang angle was parallel to the build plate. This gradual decrease in the overhang angle causes accumulation of heat as it is

progressively surrounded by the powder on the underside – the powder is a poor conductor of heat compared to a completely consolidated part. The arch-shaped parts without support were anticipated to accumulate heat near the topmost regions leading to thermal-induced distortion.

An approach to prevent the failure of arches is to build them with supports. Supports in LPBF serve two purposes. First, they provide anchoring to prevent collapse of overhanging features due to their weight. Second, supports provide a path for heat to be conducted away from a volume (termed thermal supports). Hence, the arches built with supports, labeled with the prefix SA, would tend to have reduced thermal gradients. This is because heat is rapidly conducted to the base area by the supports. Consequently, building arches with supports would mitigate the tendency for deformation and recoater crash. Indeed, of the five arches created without support, only one succeeded, while all five arches with support were completed without a recoater crash.

#### *2.2.6 Build Progress*

The build plate after completion, along with a timeline tracking its progress, is shown in Figure 5. The two cone-shaped geometries (C40 and C45), overhang geometries (O45 and O55), all supported arches (SA05, SA10, etc.,) and the N-shaped part were completed without geometry-related failures. However, only one of the five arches without supports (A15) was completed, all other arches without supports (A05, A10, A20, A25) failed to complete due to recoater crash. The total time for the build was estimated before the build (by a slicing software) to be 525 minutes (8 hours 45 minutes). However, due to three recoater crashes, the actual build time was close to 570 minutes (9 hours 30 minutes), because after each recoater crash operator intervention was needed to continue the build.

Two build transition epochs, Transition A and Transition B are marked in Figure 5. As is explained in Sec. 2.4 these transition epochs are linked to significant changes in the time elapsed

between the melting of two consecutive layers, and hence influence the cooling characteristics. The first, denoted as Transition A occurred at layer 200 (8 mm build height) where the base-sections of the parts are completed. The second transition, marked as Transition B, occurred at layer 500 (20 mm build height) on the completion of the two cone-shaped parts.

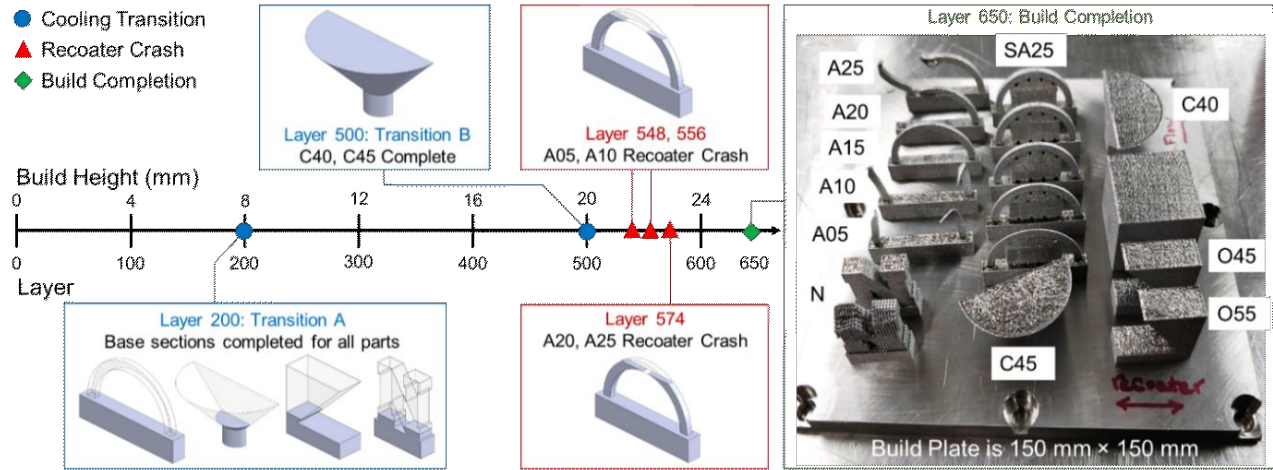


Figure 5: The completed build plate and build timeline. We observe that the arches A05, A10, A20, A25 fail in the range of layers 548 to 574. None of the arches with supports have failed.

### 2.2.7 Post- Processing Characterization

The cone-shaped and overhang geometry parts were examined using non-destructive X-ray computed tomography (XCT, Nikon XTH225 ST) at a resolution of 15  $\mu\text{m}$  per voxel. Volumetric porosity analysis was performed on the XCT images using the Volume Graphics software (VGStudio Max).

For microstructure characterization, the parts were sectioned along different planes using wire electro-discharge machining (wire-EDM). The cross-sectioned samples were ground and polished using silicon carbide abrasive paper (400, 600, 800, and 1200 grit) and fine-polished using diamond paste (3, 1, and 0.5  $\mu\text{m}$ ). The cross-sections were examined with optical microscopy to further affirm the type of porosity (lack-of-fusion or gas porosity) [6]. In preparation of scanning electron microscopy (Helios 660 NanoLab, FEI), the samples were etched with aqua regia for 10 seconds.

## 2.3 Temperature Measurements

### 2.3.1 Calibration of the Thermal Camera Readings

The temperature readings obtained by the infrared camera are not absolute temperature measurements but only depict relative trends [63-65]. The temperature recorded by an infrared thermal camera is a relative measurement that depends on the emissivity and surface roughness of the object being measured, as well the angle of incidence of the thermal camera [63-65]. Several different approaches have been devised by researchers to calibrate the thermal camera images obtained in LPBF; these are reviewed in depth by Lane and co-workers [63, 65].

In this work, we calibrated the thermal camera images to a reference thermocouple reading. The procedure, which was documented in depth in our previous publications, Ref. [49, 66], is summarized here. This calibration procedure is frequently used in LPBF as exemplified in the work of Hooper *et al.* [60] and Wicker *et al.* [67]. After the completion of the build, the powder from around the parts was cleared, and the entire build plate along with the parts was heated in a controlled manner by placing it on a specially devised fixture. The build plate stayed inside the LPBF machine, and its inclination and distance from the thermal camera was maintained identical to the actual build condition. As the build plate was heated, the temperature of the cone-shaped part C45 was measured with a thermocouple affixed to its surface.

The thermal camera readings were mapped to the thermocouple measurements by fitting a calibration function. The calibration function is shown in Figure 6. Mapped on the y-axis of Figure 6(a) are the temperature readings recorded by the thermocouple. The surface temperature measurements recorded by the IR thermal camera are plotted on the x-axis along with the  $\pm 1\sigma$  error bars. The pixel value represented in Figure 6(a) is the average of the thermal camera measurements taken over a  $9 \text{ pixel} \times 9 \text{ pixel}$  ( $\sim 4 \text{ mm}^2$ ) area on the top surface of the cone shaped-



part. This sampling region is depicted later in Figure 7(a) in Sec. 2.2.7. The dotted line in Figure 6(a) is the calibration function fitted to the data.

The calibration process was repeated with a layer of powder of  $\sim 40 \mu\text{m}$  deposited on top of the parts. Repeating the calibration procedure with powder on top of the part is important, because, as is explained shortly in Sec. 2.3.3, the end-of-cycle surface temperature as defined and used in this work is obtained after a new layer of powder is deposited. The calibration function for the solid part and with powder on top is shown below in Figure 6(b).

These calibration functions were expected to remain valid for thermal camera temperature readings beyond  $400^\circ\text{C}$ , as the emissivity would not change significantly until the melting point. In this work, the maximum surface temperature reached was  $550^\circ\text{C}$  for the cone-shaped part C40 (discounting the anomalous effect of recoater crash).

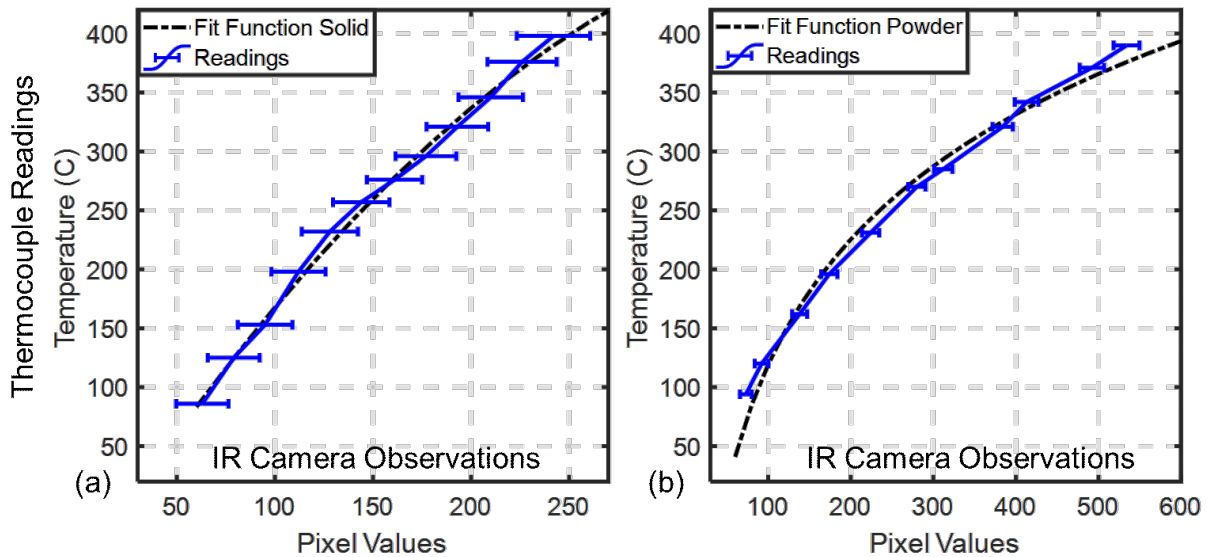


Figure 6: The calibration function for the infrared thermal camera with thermocouple readings on the y-axis, and the values observed by the thermal camera over a  $9 \text{ pixel} \times \text{pixel}$  area (error bars are 1 standard deviation long). A two-step calibration procedure is used. (a) The first step involves fitting a calibration function to the temperature of a solid part without a layer of powder on top, (b) The second calibration step involves fitting another function to the thermal camera and thermocouple readings with a layer of powder deposited on top of the part.

### 2.3.2 *Obtaining the End-of-Cycle Surface Temperature*

The procedure for obtaining the end-of-cycle surface temperature ( $t_s$ ) from the thermal images is described in the context of the cone-shaped part with  $45^\circ$  inclination angle (C45). For C45, a  $9 \text{ pixel} \times 9 \text{ pixel}$  region from the IR camera data was selected. This sampled area is annotated in Figure 7(a) and equates to a  $\sim 4 \text{ mm}^2$  area on the top surface of the part. We eschewed measurement near the edge of the part as the blur from the thermal image would lead to measurement error.

Temperature readings from the infrared thermal camera image from this  $4 \text{ mm}^2$  area were averaged to obtain a top surface temperature. The temperature trend for this sampled region over the entire build duration of C45 is shown in Figure 7(b). The cone-shaped parts were completed at layer 500, the entire build completed at layer 650. A sample of the temperature trend over three layers is shown in Figure 7(c).

From the raw temperature data shown in Figure 7(b), we extracted the end-of-cycle surface temperature in the following manner. Referring to Figure 7(c), the raw temperature has three prominent features, demarcated (A), (B), and (C), which correspond to specific process events.

At the outset we note that the thermal camera acquires data only when the laser is active through a triggering mechanism. The first large spike marked (A) is on account of the laser processing the sampled  $4 \text{ mm}^2$  pixel region. The temperature recorded at (B) is momentarily prior to the time the laser and camera are both switched off. The epoch marked (C) and beyond is for the next layer processed by the laser. In the interim between (B) and (C) the recoater fetches powder, and a fresh layer is deposited.

The time for recoating is measured to be 11 seconds, and remains fixed irrespective of the process conditions or number of parts on the build plate. The temperature in the instant just before the laser strikes the sampled area again, before the melting of a new layer, is termed as the end-of-

cycle surface temperature ( $t_s$ ). Plotted in Figure 7(d) is the end-of-cycle surface temperature for the  $9 \text{ pixel} \times 9 \text{ pixel}$  area ( $4 \text{ mm}^2$ ) of the cone-shaped part C45 sampled in Figure 7(a). The end-of-cycle surface temperature ( $t_s$ ) was compiled for each part by sampling a fixed location using the procedure described in the forthcoming Sec. 2.3.3

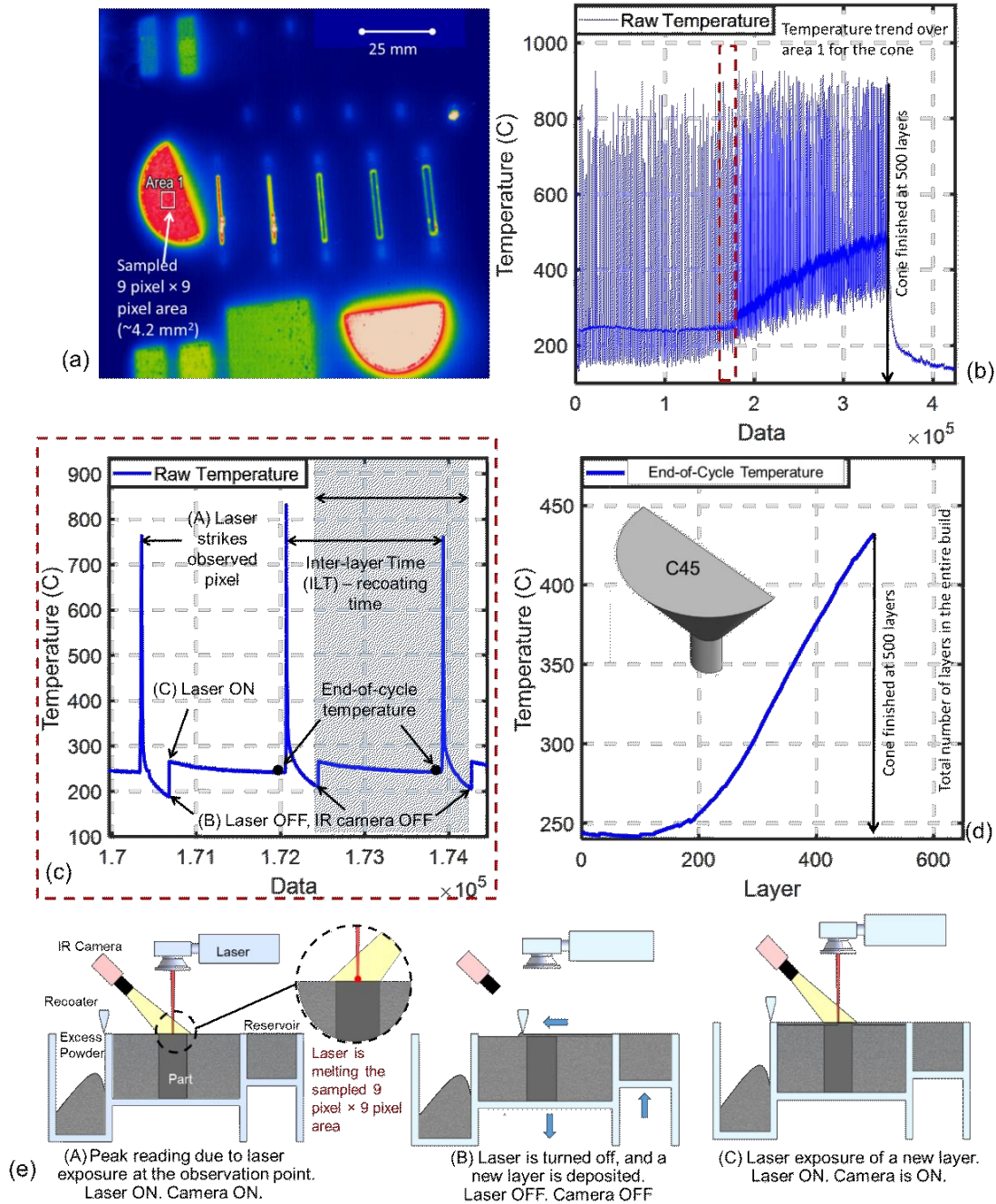


Figure 7: (a) The  $9 \text{ pixel} \times 9 \text{ pixel}$  area over which the surface temperature trends are averaged for the C45 cone-shaped test artifact. (b) The surface temperature trends for the entire duration

of the build, processing of the test part C45 is completed at layer 500. (c) The zoomed in area of the temperature trends over three cycle layers, including the end-of-cycle point where the end-of-cycle temperature is obtained. There are three prominent epochs that are observed in the temperature trends on account of process events, labeled (A) through (C) (d) the end-of-cycle surface temperature for the duration of build corresponding to C45. (e) The process events that cause the three epochs observed in the temperature trends in (c).

### 2.3.3 End-of-Cycle Surface Temperature Measurements for each Part

The sampled locations over which the end-of-cycle surface temperature was tracked for each part are shown in Figure 8. The sampled area equates to a total of  $4 \text{ mm}^2$  corresponding to 81 pixels in the image of the thermal camera for all parts except the arches. The total area sampled for the arches is  $2 \text{ mm}^2$  ( $1 \text{ mm}^2$  per arm of the arch, 20 pixels per  $\text{mm}^2$ ). The narrow cross-section of the arches prevented sampling a larger area.

These sample locations were chosen to form a single contiguous volume near the center of the part. Hence, in the case of the cone, arches, and overhang parts the sampled area follows the contour of the part. As mentioned previously, we avoided sampling the surface temperature near the part boundary owing to the limited spatial resolution of the thermal camera which would lead to image blurring. We plotted the surface temperature for each of the test geometries in Figure 9.

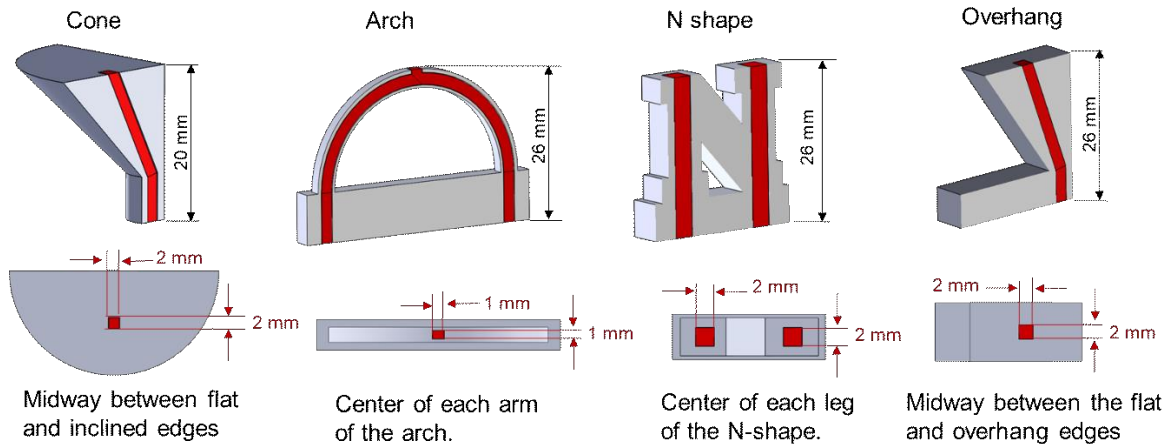


*Figure 8: The spatial locations where the end-of-cycle surface temperature of the part is averaged are shown in the context of the three dimensional view and top views. The area sampled equates to 81 pixels ( $4 \text{ mm}^2$ ) for all parts, except the arches. For the arches a  $4 \text{ mm}^2$  (20 pixels) is sampled. The sampled area is taken in the interior of the part to avoid error from blurring of the thermal camera images at the edges.*

*a) Cone-shaped Parts (C40 and C45)*

The temperature distribution for the cone shaped parts is shown in Figure 9(a). The surface area (and volume) of the cone gradually increased with the build height. In our previous work [49], we found that the increasing surface area leads to an increase in the time required by the laser to scan each layer, hence the part has a longer time to cool between layers. However, the smaller surface area of the preceding layers compared to the layer being melted impedes the rapid conduction of heat away from the surface. These two effects taken together leads to an increase in surface temperature with layer height.

Comparing the two cone-shaped parts, the cone with the overhang angle  $Z = 40^\circ$  (C40) had a larger surface area compared to the cone with  $Z = 45^\circ$  (C45). Hence, C40 had a higher surface temperature than C45. In this work, we quantified the effect of the geometry on the surface temperature distribution, and subsequently, correlated the temperature distribution with the microstructural evolution and flaw formation through metallography and X-ray computed tomography (XCT) analysis, respectively. The cone-shaped part C45 is used to calibrate the model parameters. The overhang parts are subjected to metallography and XCT analysis.

*b) Overhang parts (O45 and O55)*

The surface temperature measurements for the prismatic overhang parts are mapped in Figure 9(b). In a similar vein to the cone-shaped parts, the surface temperature for O45 was higher than O55, albeit the difference was not as stark compared to the cone-shaped parts. This is because the overhang parts O55 and O45 had a substantially large base which acted as a heat sink.

c) N-shaped part

The end-of-cycle surface temperature for the N-shaped part is shown in Figure 9(c). In the N-shaped part of the presence of the base, a more uniform cross-sectional area ensured that the rise in surface temperature was gradual compared to the cone-shaped parts. The N-shaped part is used to test the model predictions.

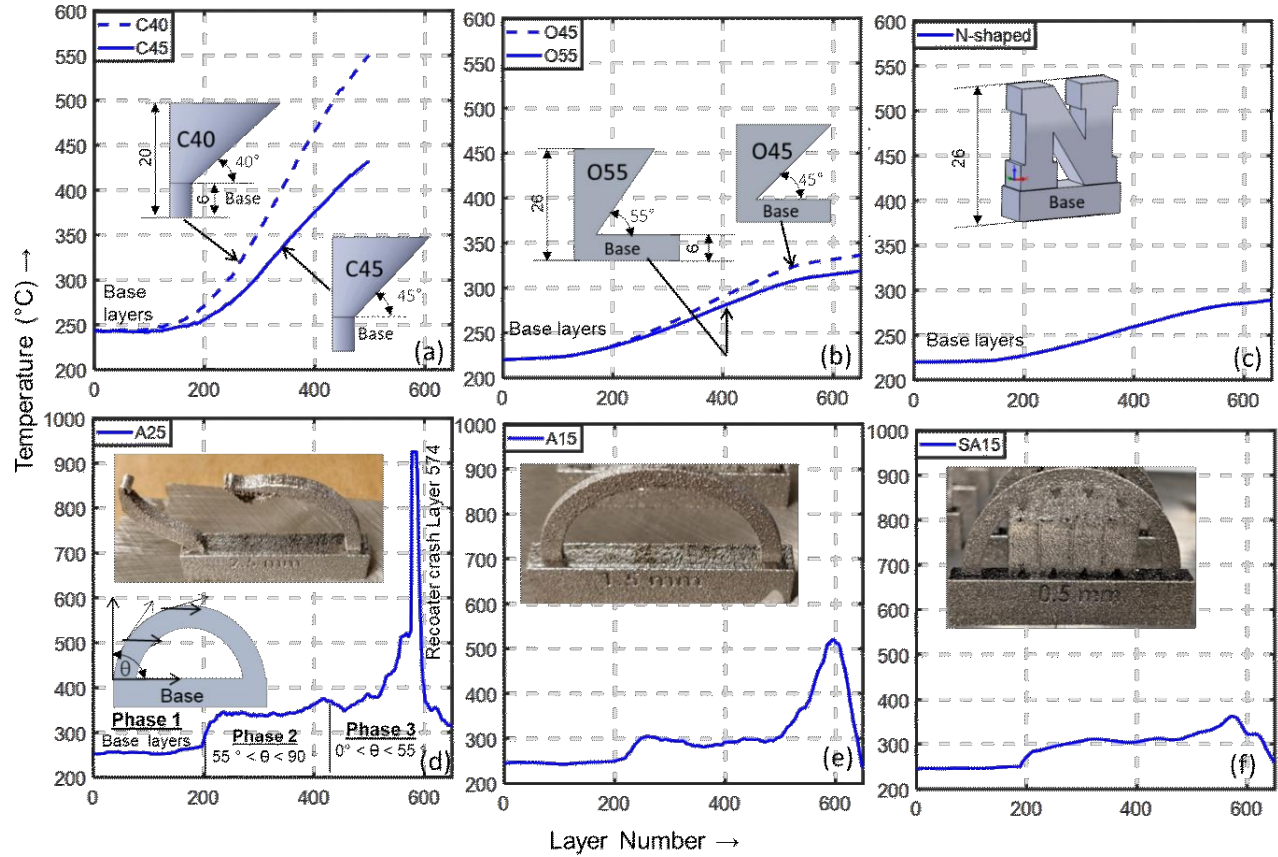


Figure 9: The end-of-cycle surface temperature distributions for the different parts.

(a) The cone C40 has a steeper temperature increase compared to the cone C45 because of its increasing surface area. (b) The effect observed in (a) is replicated in the two overhang geometries O45 and O55 albeit to a lesser degree than the cone-shaped parts.

(c) the N-shaped part shows a gradual rise in temperature as the cross-section is uniform.

(d) In the arch shaped parts without support, the overhang angle changes continually, starting at  $\theta = 90^\circ$  (vertical) to  $\theta = 0^\circ$  (horizontal) at the very top. The change in the overhang angle impedes the diffusion of heat, ultimately leading to a recoater crash. (e) The only arch-shaped part to survive was A15 which was protected by the neighboring two arches. (f) The temperature in the arch-shaped parts with support (SA) is considerably smaller than those without supports, as the heat is conducted away by the supports. All of the arches with support survived the build.

*d) Arch-shaped parts with and without supports.*

The end-of-cycle surface temperature for the arch-shaped parts is shown in Figure 9(d-f). As is described shortly, the arches without supports tend to accumulate heat which leads to superelevation (Figure 2), and ultimately causes a recoater crash. Since supports conduct heat away from the thin cross-section of the arch, the arches built with supports avoid excessive deformation and subsequent recoater crash.

The arches built without supports showed three distinct phases in the thermal history exemplified by A25 in Figure 9(d). The surface temperature was initially steady during the Phase 1 where the base section of the arches was being built (8 mm, first 200 layers). The temperature increased at Phase 2 as the base sections were completed and the relatively thin legs of the arch were built. As both legs of the arch began to curve, from layer 200 to 425 the overhang angle of the arch increased steadily decreasing from  $90^\circ$  to  $\sim 55^\circ$  with respect to the horizontal. The surface temperature during Phase 2 was largely steady around  $350^\circ\text{C}$ .

In Phase 3, the temperature history of the arch was observed a significant rise from layer 500 onwards where the cone-shaped parts are completed and overhang angle of the arch dipped below  $55^\circ$  (with respect to the horizontal) and reached its summit where the arch is almost horizontal. The temperature increased sharply in this region from  $350^\circ\text{C}$  to over  $500^\circ\text{C}$  within 100 layers. The steep temperature gradient and uneven distribution of temperature in Phase 3 caused the part to deform. The thermal-induced distortion of the arches is liable to manifest in superelevation, (i.e., the part protrudes above the powder bed and interferes with the motion of the recoater [reocater crash]).

To recover from a recoater crash, the operator must interrupt the process, and manually remove the debris of the failed part. In the layer with the collapsed arches, a sharp rise in

temperature is observed in Figure 9(d) as the laser is only scanning over powder without any underlying consolidated part – the heat does not have a conduction path to escape.

All the arches without supports A05, A10, A20 and A25 failed to build but A15 survived. A hypothesis for the arch A15 having survived the build is as follows: the large superelevation of the neighboring arches A20, A25, A10, and A05, which failed to build on account of superelevation and subsequent recoater crash, are located on either side of A15 on the build plate. The superelevation of the neighboring arches caused the recoater to flex upwards creating a small gap in the region of A15, protecting it from contact with the recoater. Hence, the surface temperature is observed in Figure 9(e) for A15 does not show the sudden spike characteristic of recoater crash.

Lastly, the arches built with support, such as SA15 shown in Figure 9(f), did not depict a sharp temperature gradient in the third phase. This is because the support structure acted as a thermal pathway for the heat to be conducted away. While Figure 9(e) shows the results for SA15, all the arches built with support had a similar thermal profile – the temperature did not increase beyond 500 °C.

#### **2.4 Estimation of the time between layers (inter-layer time, ILT).**

A key input to a thermal model of the LPBF process is the time elapsed between two layers. In this work, the time elapsed between layers for melting the sampled area shown in Figure 7(c) is called the inter-layer time (ILT). The ILT can be obtained from the G-code (the machine language which encodes the processing parameters to build the part) as well as measured from the infrared camera. The ILT plotted with dotted lines in Figure 10 is the *theoretical* ILT obtained from the G-code before the build was started. The theoretical ILT assumes that there is no recoater crash or process failures that will interrupt the build. As such, the theoretical ILT is the ideal case scenario.

Overlaid on the theoretical ILT in thick lines in Figure 10 is the *experimental* ILT estimated from the thermal camera images, using the procedure described in Sec. 2.3.2 in the context of



Figure 7(c). The experimental ILT was obtained as follows. The experimental ILT is the time interval between two large upward peaks (A) shown in Figure 7(c) + 11 seconds of recoat time (constant) + 5 seconds of enforced delay between layers before switching on the thermal camera. The five second delay is added for three reasons: (1) to provide sufficient time for a script to transfer thermal images from the limited onboard memory of the infrared camera to the hard drive of a dedicated computer, (2) to ensure complete exhausting of gaseous byproducts from the melting of the previous layers, and (3) to allow the laser galvanometric mirror to cool and for its motion to reach a resting state before the next layer is scanned.

The recoating speed remains fixed irrespective of the process conditions or number of parts on the build plate and is in accordance with commercial systems. The recoater speed used in this work is  $50 \text{ mm}\cdot\text{s}^{-1}$ , which is identical to the recoater speed used in the commercial LPBF systems made by EOS, and is considered a safe recoating speed. Faster recoating speed is liable to cause improper deposition and poor packing of the powders. Slower recoating speed reduces the process efficiency (increasing time), and also alters the cooling rate.

Two prominent transitions where the ILT are observed during the build process, one at layer 200, and another at layer 500. These changes, labeled Transitions A and B, respectively, in Figure 5, were caused by large geometry-related changes to the build at those layers. These geometry transitions changed the time to process the entire layers. These transitions are best understood in the context of the build timeline, shown previously in Figure 5, and in greater detail in Figure 10. Shown in Figure 10 is the build progression in terms of the CAD slices and the corresponding thermal images for the build for four different layers, 200, 201, 500 and 501.

At Transition A, which occurred at layer 200 to 201, the base of the arches which has a large surface area, as well as the rest of the parts studied in this work were completed. At Transition B

(layer 500 to 501), the cone-shaped parts (C40 and C45) were fully built – the cone-shaped parts had the largest surface area of all the parts. Because the cone-shaped parts C40 and C45 were no longer involved in the build, there was a sharp drop in the time required to scan a layer, which led to a decrease in the time between layers (inter-layer time, ILT).

As observed in Figure 10, prior to the first recoater crash observed in layer 548, the ILT obtained from the machine G-code (theoretical ILT) and the ILT estimated from the thermal camera (experimental ILT) are nearly identical. It takes almost 15 minutes to reset the machine after the recoater crash, and consequently, the ILT observed after the recoater crash is not shown. Since, our aim is to predict the surface temperature *before* the part is built, we use the theoretical ILT in the graph theory model.

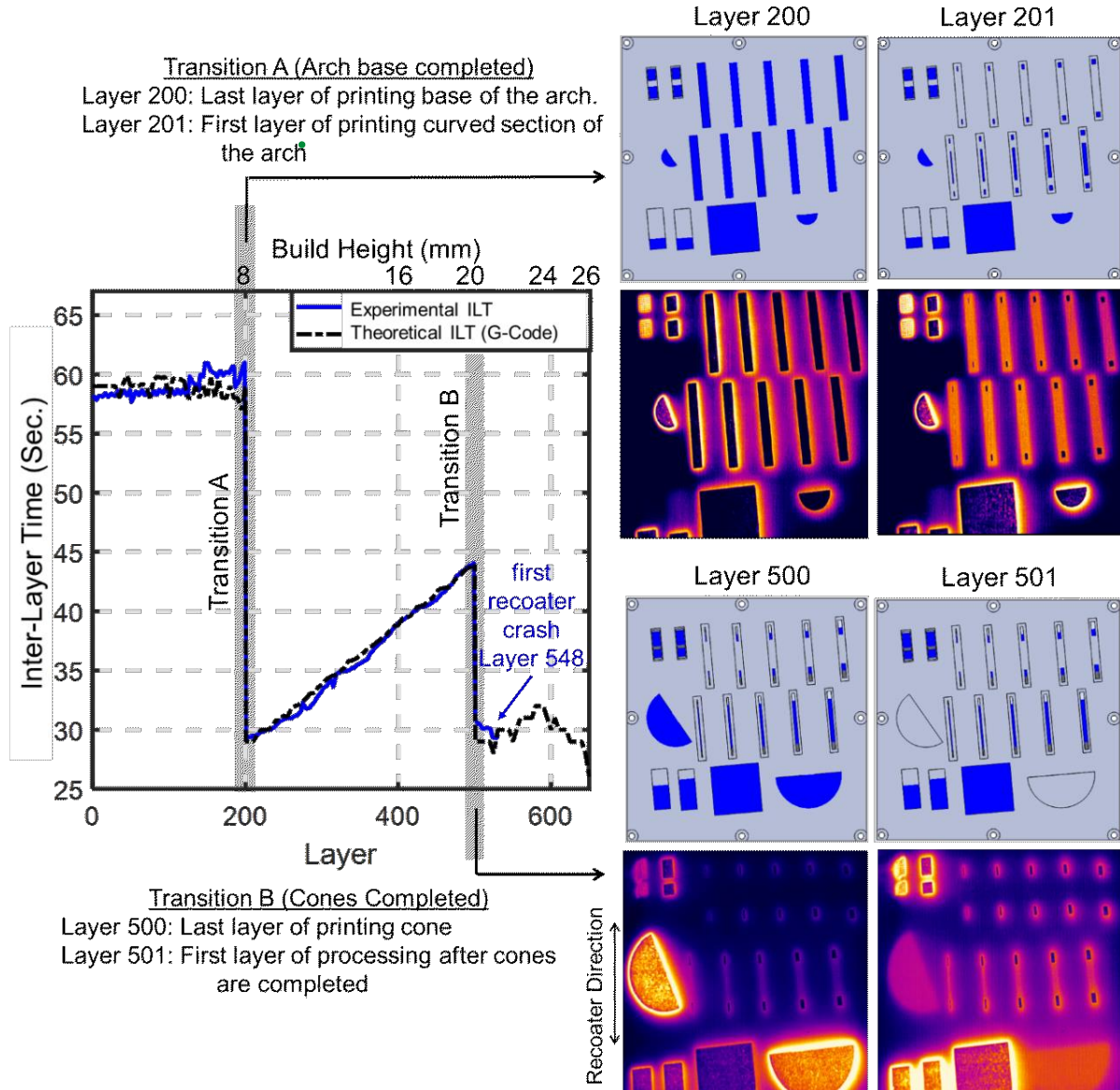


Figure 10: The inter-layer time (ILT) for the entire part. The theoretical ILT (dotted black line) is calculated directly from the G-code and therefore presents the ideal state. The experimentally observed ILT (thick blue line) is estimated from the thermal camera data. The practical and theoretical ILT agree closely, until the point of the first recoater crash at layer 548. Once a recoater crash occurs, the operator has to manually reset the recoater, a process that takes several minutes. Hence, after layer 548 the experimental ILT is no longer consistent with theoretical ILT. There are two transitions at layer 200 and 500. These are explained based on the CAD slices and corresponding thermal images for layers 200, 201, 500, and 501. At layer 200 (8 mm build height) the large base layers for all parts are completed. The ILT drops after layer 200 as the scan area is reduced. The next transition occurs at layer 500 (20 mm build height), after the two cone-shaped is completed.

### 3.1 The graph theory approach to solve the heat diffusion equation.

The temperature distribution in the LPBF is predicted by solving the continuum *heat diffusion equation* [68]. In LPBF and metal AM in general, FE analysis is popularly used to solve the heat diffusion equation and obtain the temperature history [68].

$$\begin{array}{c} \text{Material} \\ \text{Properties} \\ \overline{\rho c_p} \end{array} \frac{\partial T(x, y, z, t)}{\partial t} - k \overbrace{\left( \frac{\partial^2}{\partial x^2} + \frac{\partial^2}{\partial y^2} + \frac{\partial^2}{\partial z^2} \right)}^{\text{Laplacian (part shape)}} T(x, y, z, t) = \begin{array}{c} \text{Processing} \\ \text{Parameters} \\ \overline{E_v} \end{array} \quad (1)$$

where  $E_v = \frac{P}{v \times h \times t}$

Here  $T$  is the temperature rise above the ambient temperature. The accompanying initial and boundary conditions are given by,

$$T(x, y, z, 0) = 0 \text{ (initial condition)}$$

$$\frac{\partial T}{\partial n} = 0 \text{ (on boundary)} \quad (2)$$

where  $n$  is the outward normal vector at the boundary. Although this boundary condition is for zero heat loss, the effect of external heat loss by convection and radiation is discussed in Section 3.2 as an adjustment to the graph theory method.

Solving the heat diffusion equation subject to the accompanying conditions results in the temperature  $T(x, y, z, t)$  for a location  $(x, y, z)$  at a time instant  $t$  inside a part, which is the thermal history. The term  $E_v$ , called energy density [ $\text{J} \cdot \text{m}^{-3}$ ], is the energy supplied by the laser to melt a unit volume of material. The energy density  $E_v$  is a function of laser power ( $P$ ) [ $\text{W}$ ], distance between adjacent passes of the laser ( $h$ ) [ $\text{m}$ ], translation velocity ( $v$ ) [ $\text{m} \cdot \text{s}^{-1}$ ], and the layer thickness ( $t$ ) [ $\text{m}$ ]; these are the controllable parameters of the LPBF. The material properties are density  $\rho$  [ $\text{kg} \cdot \text{m}^{-3}$ ], specific heat  $c_p$  [ $\text{J} \cdot \text{kg}^{-1} \cdot \text{K}^{-1}$ ], and thermal conductivity  $k$  [ $\text{W} \cdot \text{m}^{-1} \cdot \text{K}^{-1}$ ]. The effect of the

part shape on the temperature is embodied in the second derivative term, called the *continuous Laplacian*. The material properties,  $\rho$ ,  $c_p$  and  $k$  are assumed to be constant.

Meshing of the part geometry is the computationally time-consuming aspect of FE-based thermal analysis in LPBF. This is because the part shape changes continually with deposition of each new hatch or layer and has to re-meshed [69-71]. Although commercial software packages have pioneered techniques to reduce the computational burden, for example adaptive meshing, such algorithms are proprietary [46]. The graph theory approach reduces the computational burden by solving a discrete version of the heat diffusion equation in the following manner.

As in existing FE approaches, the laser energy density  $E_v$  in Eq. (1) is replaced by an initial temperature distribution caused by the laser,  $T_o(x, y, z)$ . Then the heat diffusion equation and the accompanying conditions become,

$$\frac{\partial T}{\partial t} - \alpha \left( \frac{\partial^2}{\partial x^2} + \frac{\partial^2}{\partial y^2} + \frac{\partial^2}{\partial z^2} \right) T = 0 \quad (3)$$

$$T(x, y, z, 0) = T_o(x, y, z) \quad (\text{initial condition})$$

$$\frac{\partial T}{\partial n} = 0 \quad (\text{on boundary}) \quad (4)$$

where  $\alpha = k/(\rho c_p)$  is the thermal diffusivity,  $\alpha$  [ $\text{m}^2 \cdot \text{s}^{-1}$ ].

Next, the heat diffusion equation is discretized over  $N$  nodes by replacing the second order derivative (continuous Laplacian) with the discrete *Laplacian Matrix* ( $L$ ) and by replacing the continuous temperature by a discrete temperature vector:

$$\frac{\partial T}{\partial t} + \alpha L T = 0 \quad (5)$$

The eigenvector matrix ( $\Phi$ ) and eigenvalue matrix ( $\Lambda$ ) of the Laplacian matrix ( $L$ ) are found by solving the eigenvalue equation  $L\Phi = \Phi\Lambda$ . As the Laplacian matrix is symmetric and positive semi-definite, as described later in Section 3.2, the eigenvalues ( $\Lambda$ ) are non-negative, and the

eigenvector matrix ( $\Phi$ ) is orthogonal [72-75]. As the transpose of an orthogonal matrix is the same as its inverse, that is,  $\Phi^{-1} = \Phi'$  and  $\Phi \Phi' = I$ , where  $I$  is the identity matrix, then the eigenvalue equation  $L\Phi = \Phi\Lambda$  may be post-multiplied by  $\Phi'$  to obtain  $L = \Phi\Lambda\Phi'$ . Substituting  $L = \Phi\Lambda\Phi'$  in Eq. (3) gives,

$$\frac{\partial T}{\partial t} + \alpha(\Phi\Lambda\Phi') T = 0 \quad (6)$$

Equation (6) is a first order, ordinary linear differential equation, with solution [61],

$$T = e^{-\alpha(\Phi\Lambda\Phi')t} T_o \quad (7)$$

The term  $e^{-\alpha(\Phi\Lambda\Phi')t}$  is simplified via a Taylor series expansion and substituting  $\Phi \Phi' = I$ ,

$$\begin{aligned} e^{-\alpha(\Phi\Lambda\Phi')t} &= I - \frac{\Phi\Lambda\alpha t\Phi'}{1!} + \frac{(\Phi\Lambda\alpha t\Phi')^2}{2!} - \frac{(\Phi\Lambda\alpha t\Phi')^3}{3!} + \dots \\ &= I - \frac{\Phi\Lambda\alpha t\Phi'}{1!} + \frac{(\Phi\Lambda\alpha t\Phi')(\Phi\Lambda\alpha t\Phi')}{2!} - \frac{(\Phi\Lambda\alpha t\Phi')(\Phi\Lambda\alpha t\Phi')(\Phi\Lambda\alpha t\Phi')}{3!} + \dots \\ &= I - \frac{\Phi\Lambda\alpha t\Phi'}{1!} + \frac{\Phi'(\Lambda\alpha t)^2\Phi'}{2!} - \frac{\Phi(\Lambda\alpha t)^3\Phi'}{3!} + \dots \\ e^{-\alpha(\Phi\Lambda\Phi')t} &= \Phi e^{-\alpha(\Lambda)t} \Phi' \end{aligned} \quad (8)$$

Substituting,  $e^{-\alpha(\Phi\Lambda\Phi')t} = \Phi e^{-\alpha\Lambda t} \Phi'$  into Eqn. (6) gives,

$$T = \Phi e^{-\alpha\Lambda t} \Phi' T_o \quad (9)$$

Equation (9) is the graph theory solution to the discrete heat diffusion equation as a function of the eigenvalues ( $\Lambda$ ) and eigenvectors ( $\Phi$ ) of the Laplacian Matrix ( $L$ ), constructed on a discrete set of nodes. The graph theory approach has two inherent advantages over FE analysis.

- (1) *Elimination of mesh-based analysis.* The graph theory approach represents the part as discrete nodes, which entirely eliminates the tedious meshing steps of FE analysis.
- (2) *Elimination of matrix inversion steps.* While FE analysis rests on matrix inversion at each time-step for solving the heat diffusion equation, the graph theory approach relies on matrix multiplication, shown in Eq. (9), which greatly reduces the computational burden.

We now briefly describe the manner in which the graph theory approach is adapted for thermal modeling in LPBF.

### 3.2 Application of graph theory-based thermal modeling to LPBF

The graph theory approach is illustrated schematically in Figure 11 in the context of the arch-shaped parts without supports.

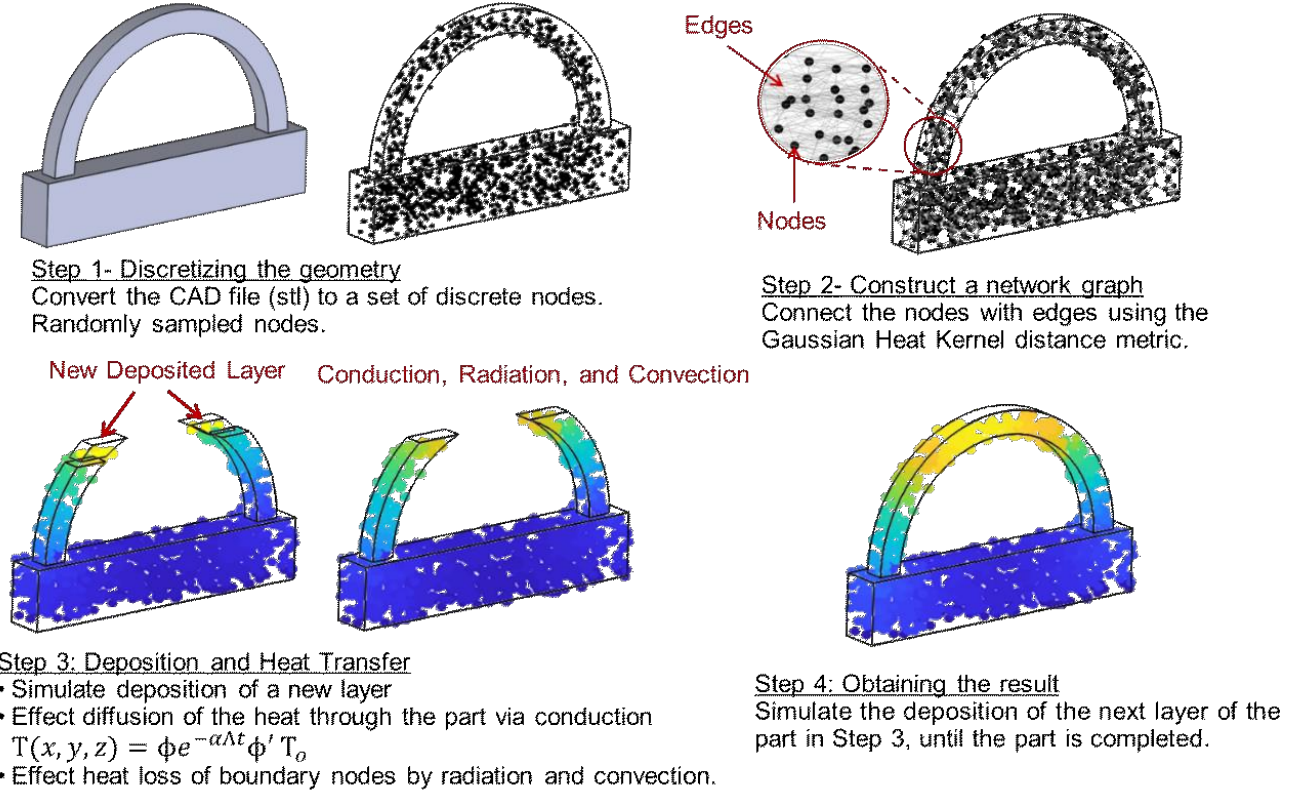


Figure 11: Schematic representation of the graph theory approach for the test case of the arch without support. There are four main steps in the approach.

#### **Step 1: Represent the part's geometry in terms of randomly sampled nodes.**

The key idea of the graph theory approach is to convert the part geometry into a number of discrete nodes [48]. First, the part geometry in the form of the STL file is converted into a set of discrete nodes, and a fixed number of  $N$  nodes will be sampled randomly. The position of these  $N$  nodes will be recorded in terms of their spatial coordinates  $(x, y, z)$ . In the ensuing steps, the temperature at each time step will be stored at these nodes.

#### **Step 2: Construct a network graph by connecting nodes using the heat kernel.**

In this step, the sampled nodes are connected based on their distance. Consider a node  $\pi_i$  whose Cartesian coordinates are  $c_i \equiv (x_i, y_i, z_i)$ . We envelope a sphere of radius  $\varepsilon$  [mm] centered on the node  $\pi_i$ . The *neighborhood distance* ( $\varepsilon$ ) is set less than the smallest dimension feature of the part called the *characteristic length*. In this work,  $\varepsilon = 2$  mm to accommodate the arch-shaped part. Setting the neighborhood distance prevents the connection of nodes across the part-powder boundary.

Next, within this  $\varepsilon$ -neighborhood, we connect the node  $\pi_i$  to only its five nearest nodes with an edge. The distance between  $\pi_i$  and a node  $\pi_j$  whose spatial Cartesian coordinates  $c_j \equiv (x_j, y_j, z_j)$  is the Euclidean distance  $\|c_i - c_j\| = \sqrt{(x_i - x_j)^2 + (y_i - y_j)^2 + (z_i - z_j)^2}$ .

Further, for nodes that are connected, and the connection itself is called an *edge*, we assign a weight. The edge weight  $a_{i,j}$  is given by,

$$\begin{aligned} a_{i,j} &= e^{-\frac{\|c_i - c_j\|^2}{\sigma^2}} & \forall i \neq j \\ a_{i,j} &= 0 & \forall i = j \end{aligned} \quad (10)$$

No node is connected to itself. The edge weight,  $a_{i,j}$  represents the normalized strength of the connection between the nodes  $\pi_i$  and  $\pi_j$  and has a value between 0 and 1. Quantity  $\sigma^2$  in Eq. (10) is the variance of the Euclidean distance between all node pairs.

The closer a node  $\pi_i$  is to another  $\pi_j$ , exponentially stronger is the connection ( $a_{i,j}$ ) and hence proportionally greater is the heat transfer via conduction between the two nodes [73, 74, 76]. The edge weight in graph theory, unlike FE methods, only depends on the distance between nodes. In contrast the FE-approach requires node-to-node spatial orientation, which is computationally demanding and requires a time-consuming meshing step. The key aspect of the graph theory approach is that it completely eliminates this meshing step.



Next, the matrix formed by placing  $a_{ij}$  in a row  $i$  and column  $j$  is called the adjacency matrix,  $A = [a_{i,j}]$ .

$$A = \begin{bmatrix} 0 & a_{1,2} & a_{1,3} & \cdots & a_{1,N} \\ a_{2,1} & 0 & a_{2,3} & \cdots & a_{2,N} \\ a_{3,1} & a_{3,2} & 0 & \cdots & a_{3,N} \\ \vdots & \vdots & \vdots & \ddots & \vdots \\ a_{N,1} & a_{N,2} & a_{N,3} & \cdots & 0 \end{bmatrix} \quad (11)$$

The adjacency matrix is an  $N \times N$  symmetric matrix, as  $a_{i,j} = a_{j,i}$ , where  $N$  represents the number of nodes in the part. From the adjacency matrix ( $A$ ), the degree matrix ( $D$ ) is obtained by summing the rows (or columns of  $A$ ), in the following manner.

$$d_{i\cdot} = \sum_{j=1}^N a_{i,j}$$

$$D = \begin{bmatrix} d_{1\cdot} & 0 & 0 \\ 0 & \ddots & 0 \\ 0 & 0 & d_{N\cdot} \end{bmatrix} \quad (12)$$

In the degree matrix  $D$ , all the off-diagonal entries are zero and the diagonal entries  $d_{i\cdot}$  are positive. Next, the discrete graph Laplacian matrix is obtained as  $L = D - A$ , as follows:

$$L = \begin{bmatrix} +d_{1\cdot} & -a_{1,2} & -a_{1,3} & \cdots & -a_{1,N} \\ -a_{2,1} & +d_{2\cdot} & -a_{2,3} & \cdots & -a_{2,N} \\ -a_{3,1} & -a_{3,2} & +d_{3\cdot} & \cdots & -a_{3,N} \\ \vdots & \vdots & \vdots & \ddots & \vdots \\ -a_{N,1} & -a_{N,2} & -a_{N,3} & \cdots & +d_{N\cdot} \end{bmatrix} \quad (13)$$

The Laplacian matrix is symmetric and diagonally dominant, therefore all its eigenvalues are non-negative and its eigenvectors are orthogonal [77, 78].

***Step 3: Simulate melting of each layer and predict the temperature distribution.***

In this step the layer-by-layer deposition and heating of the part by the laser is simulated. The heat on the top layer, introduced by the scanning laser, diffuses to the rest of the part. The temperature

at each node is determined at time  $\tau$  following the laser heating of the top layer. The time period of interest ( $\tau$ ) is the inter-layer time (ILT), and the temperature at this time is obtained as a function of the Laplacian eigenvectors ( $\phi$ ) and eigenvalues ( $\Lambda$ ), and initial temperature distribution in the part  $T_0$ :

$$T(x, y, z, \tau) = \phi e^{-\alpha g \Lambda \tau} \phi' T_0(x, y, z) \quad (14)$$

In this work, the peak value of the initial temperature distribution is the melting point of Inconel 718,  $T_0 = \sim 1400$  C, and the time  $\tau$  is the theoretical ILT from Figure 10. In practice, we simulate the deposition and melting of several layers at once, called the superlayer or meta-layer approach. Hence the ILT is averaged over multiple layers.

A parameter called the gain factor  $g$  is included in Eq. (10) to adjust the units. We have discussed the effect of the gain factor  $g$  in our previous work, and accordingly selected  $g = 2 \times 10^5 \text{ m}^{-2}$  [48].

Thus, from Eq. (14), the temperature of the nodes is determined considering heat diffusion within the object. Next, heat loss for nodes on the boundary of the object is included. The nodes at the boundary experience heat loss due to radiation and convection. The temperature of the boundary nodes ( $T_b$ ) is adjusted using lumped capacitive theory,

$$T_b = e^{-\tilde{h}\tau} (T_{bi} - T_p) + T_p \quad (15)$$

Here  $T_p$  is the temperature of the surroundings,  $T_{bi}$  is the temperature of the boundary node found by heat diffusion alone,  $T_b$  is the temperature of the boundary node following external heat loss,  $\tau$  is the dimensionless time between laser scans, and  $\tilde{h}$  is the normalized combined coefficient of radiation (via Stefan-Boltzmann law) and convection (via Newton's law of cooling) from the boundary to the surroundings [79].

***Step 4: Repeat Steps 3 for each layer until the build process is complete.***

The layer-by-layer deposition of the part is simulated by repeating Step 3. After the end of each simulation of each layer, the temperature at each node is found in matrix form  $T$ . Then this temperature is altered by the addition of newly added material at the metal-melting point, which becomes the initial condition for the graph theory simulation of the next interlayer period, followed by the next, and so on.

Temperature predictions from graph theory are given by vector  $T$  containing temperature at every node in the volume of the part. In recent work by the authors, the temperature in the interior of a part obtained from graph theory, finite element, and finite difference methods were shown to compare favorably [47, 49]. However, in this work, only the surface temperature is used for validating the predictions from the graph theory approach.

### *3.2.1 Model Assumptions*

1. The shape of the laser is ignored – a double ellipsoid shape of the laser is a typical assumption in FE-based models. In the graph theory approach the laser is assumed to be a moving point source of heat [34, 35].
2. As in FE-based models, to reduce computation time, the graph theory approach makes the meta-layer or superlayer approach, wherein multiple layers of material are assumed to be deposited at once. Although the graph theory approach is capable of hatch-level resolution.
3. The effect of temperature on material properties, such as specific heat and density are ignored. The effect of latent heat of fusion on account of the material changing from powder (solid) to liquid, and again back to solid is not accounted.

### **3.3 Prior Work Applying Graph Theory in LPBF**

In our prior works, we showed that the temperature distribution in LPBF parts is predicted using graph theory with accuracy comparable to existing FE-based models but within a fraction of

the time [47-49]. In Ref. [47], the mathematical foundations of the graph theory approach was established and the concept was applied to one- and three-dimensional benchmark heat transfer problems. The predictions from the graph theory approach were observed to be accurate within 2% of the exact analytical solution and converged in less than 20% to 30% of the time required by FE analysis.

Next, in Ref. [48], the graph theory approach was applied to the LPBF process. In that paper we simulated the LPBF of three rudimentary prismatic shapes. The thermal history at various points inside the part were predicted from the graph theory approach, and compared with predictions from Goldak's double ellipsoid FE-based model [48]. The graph theory approach converged to an identical level of accuracy as that of the FE solution, but within 10% of the time (18 minutes versus 3 hours). This paper also qualitatively compared the result with those from the commercial Autodesk Netfabb simulation software.

In Ref. [49] the graph theory thermal predictions were compared with experimental temperature data obtained using an in-situ infrared thermal camera. These tests included cylindrical and cone-shaped LPBF parts. These prior results affirmed that the graph theory-derived thermal history converged to an identical prediction error as FE analysis but within  $1/10^{\text{th}}$  to  $1/3^{\text{rd}}$  of the time. Recently, we extended the graph theory approach to accommodate a large volume impeller part [66].

The current paper takes these previous finding forward in two ways that are important from a practical standpoint. First, the graph theory approach is used to predict the thermal history multiple parts built at the same time on a LPBF machine as opposed to one part at a time. Second, the thermal history predictions are correlated with build failures and flaw formation.

We used the graph theory approach to predict the thermal history of the fifteen different LPBF parts processed simultaneously. Subsequently, we linked the thermal history predictions to flaw formation, porosity, microstructure heterogeneity, and recoater crash.

## 4.1 Cone Shaped Parts

### 4.1.1 Model Calibration and Performance

As described in the context of Figure 5, the two cone shaped parts C40 and C50 were completed within 500 layers (20 mm). The rest of the part shapes had a build height of 650 layers. Since there were no recoater crashes recorded during processing of the cone-shaped parts, the surface temperature distribution acquired for the cone-shaped parts was ideal for calibrating the graph theory model.

Two parameters are tuned during model calibration, namely, (i) the number of superlayers (meta-layers) that are deposited at once to speed computation, and (ii) the density of nodes (nodes per  $\text{mm}^3$ ). We used the data acquired for the cone-shaped part C45 for model calibration. There is a third parameter, called the gain factor ( $g$ ), which is dependent on the node density and material, we fixed  $g = 2 \times 10^5 \text{ m}^{-2}$  based on our previous studies in LPBF [48, 49].

The model calibration results are shown in Figure 12. The effect of increasing the model resolution by reducing the superlayer thickness (SLT) leads reduces the model prediction error as evident in Figure 12(a) and (c), at the expense of computation time. The model error with respect to the experimental data was quantified in terms of the mean absolute percentage error (MAPE) and the root mean squared error (RMSE,  $^{\circ}\text{C}$ ). In a similar vein, increasing the node density decreased the prediction error [48, 49].

A summary of the model error as a function of superlayer thickness and number of nodes is provided in the Appendix. The superlayer thickness was fixed at 0.5 mm (1 mm = 25 actual layers),

and number of nodes was set at 1 node per  $\text{mm}^3$ , the obtained MAPE was less than 3%, with RMSE  $\sim 5^\circ\text{C}$ , and the simulation converged within 2 minutes (113 seconds). With these simulation parameters, the results for both C40 and C45 are overlaid on the experimental measurements in Figure 13. There is a marked difference in the surface temperature, with C40 depicting a much steeper rise in temperature compared to C45. The uncertainty in simulation results is bounded in Figure 13, it is the  $\pm 1\sigma$  bound over ten replications.

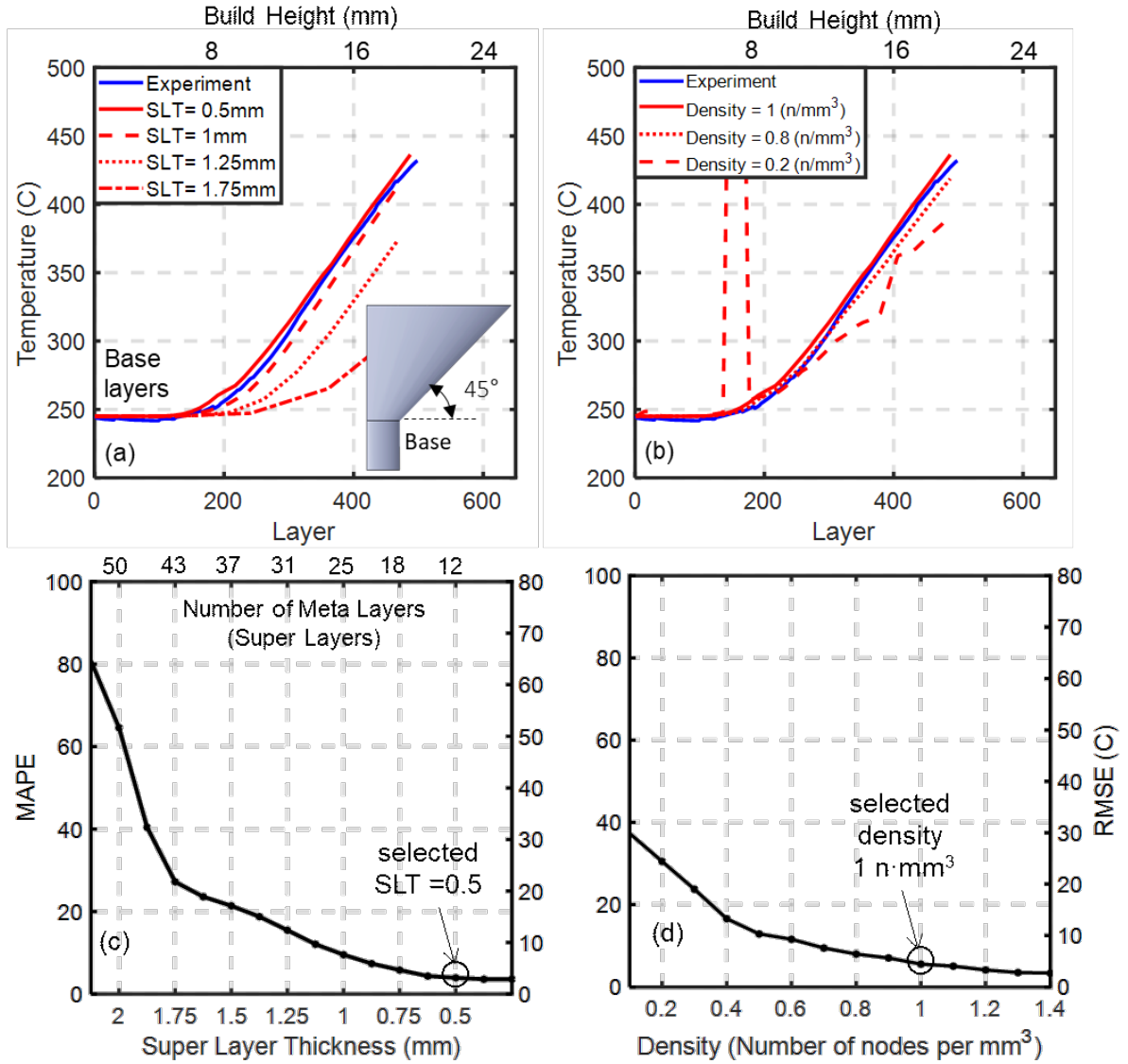


Figure 12: Calibration of the graph theory model for C45 (a and c) reducing the number of superlayers, also called superlayer thickness (SLT) improves the prediction accuracy. (b and d) the prediction error decreases with increasing node density. As a tradeoff between computation time, in this work we selected the SLT = 0.5 mm and node density as 1 node per  $\text{mm}^3$ .

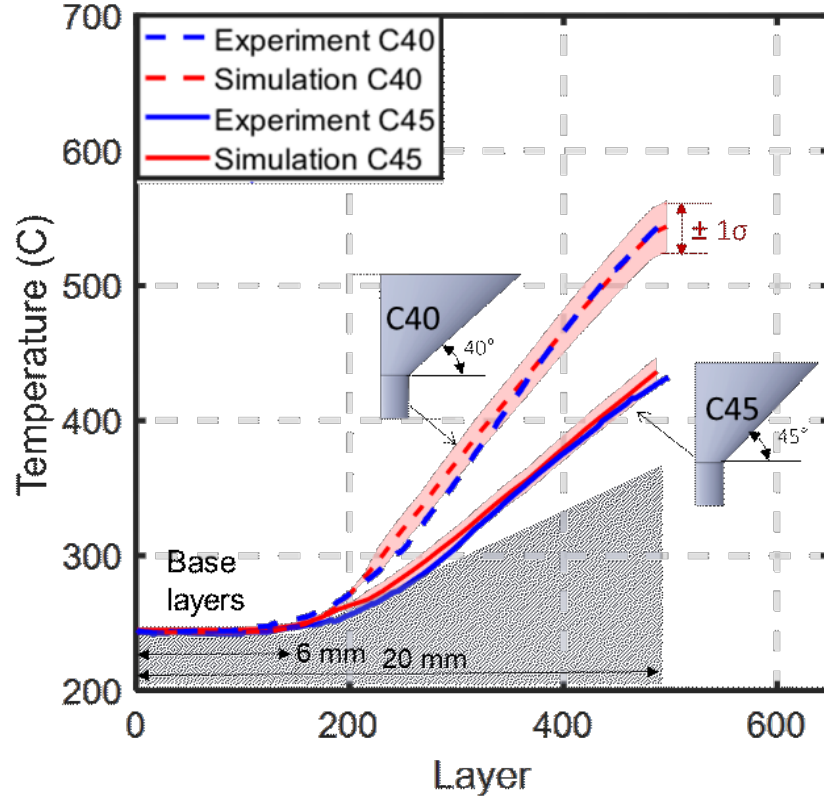


Figure 13: The temperature distribution (thermal history) for the two cone shaped parts. The parts are completed in 500 layers. The cone-shaped part C40 has a steeper temperature profile owing to its increased surface area. The red line in the figure is the thermal history predicted using the graph theory approach with  $\pm 1$  standard deviation over 10 replications, and the blue line represents the observed temperature at the sampled point obtained from the thermal camera.

Table 3. Summary of simulation parameters.

Simulation Parameters	Values
Convection coefficient wall to powder, $h_w$ [ $\text{W} \cdot \text{m}^{-2} \cdot \text{C}$ ]	$1 \times 10^{-5}$
Convection coefficient substrate (sink), $h_s$ [ $\text{W} \cdot \text{m}^{-2} \cdot \text{C}$ ]	$1.1 \times 10^{-2}$
Thermal diffusivity ( $\alpha$ ) [ $\text{m}^2/\text{s}$ ]	$3.2 \times 10^{-6}$
Density, $\rho$ [ $\text{kg}/\text{m}^3$ ]	8,190
Melting Point ( $T_0$ ) [C]	1,400
Ambient chamber temperature, $T_p$ [C]	110
Characteristic length [mm]	2
Neighborhood distance ( $\epsilon$ ) [mm]	2
Fixed number of nearest neighbors (n)	5
Superlayer thickness [mm]	0.5 (12 actual layers)
Gain factor (g) [ $\text{m}^{-2}$ ]	$2 \times 10^5$
Computational hardware	Intel Core i7-6700 CPU, @3.40 GHz with 32 GB RAM.

#### 4.1.2 Porosity Analysis

The porosity resulting from the change in the overhang angle for the two cone-shaped parts C40 and C45 is shown in Figure 14 in terms of the XCT and optical micrographs. A prominent difference in the pore type and severity are noted. For C40, uniform circular pores were observed, termed gas porosity, which are likely to be caused by escape of gas entrapped in the meltpool [6, 80]. In the case of C45, the pores were large, acicular-shaped, typical of lack-of-fusion.

As explained by Snow *et al.* [6] and Cooke *et al* [80], systemic lack-of-fusion porosity in LPBF results from poor consolidation of the material on account of insufficient input energy to fuse the material. On the other hand, excess heat would lead to gas or pinhole porosity due to the release of gas trapped in the powder material during its manufacturing process (gas or water-based atomization) or due to the release of process gasses dissolved in the meltpool. In the extreme case when the input energy density is inordinately high (high power and low velocity) keyhole porosity may result. The heat retention in C40 is advantageous as it aids material consolidation, and thus mitigates the lack-of-fusion pores observed in C45. Demarcation of the different regimes in LPBF as a function of laser power and velocity have been tendered by Gaikwad *et al.* [81].

We quantify the percentage porosity and volume distribution of the pores in Table 4 and Figure 15, respectively. This data was obtained using the Volume Graphics software. The percentage porosity for C40 was  $\sim 0.015\%$ , compared to  $\sim 1.3\%$  for C45. Moreover, the volume of the individual pores for C40 was a magnitude smaller than the pore volume for C45. For instance, the pore distribution for C40 in Figure 15 peaks at  $2.5 \times 10^4 \mu\text{m}^3$  whereas the distribution for C45 peaks at  $3.7 \times 10^4 \mu\text{m}^3$ . In effect, C45 had larger and more pores compared to C40. Hence, the porosity for the two parts was not only different in magnitude but also was caused by distinctive



phenomena. As revealed by the accompanying XCT image in Figure 15, C40 has few pores of diameter in the range of 20 to 40  $\mu\text{m}$ , whereas C45 has pores as large as 500  $\mu\text{m}$ .

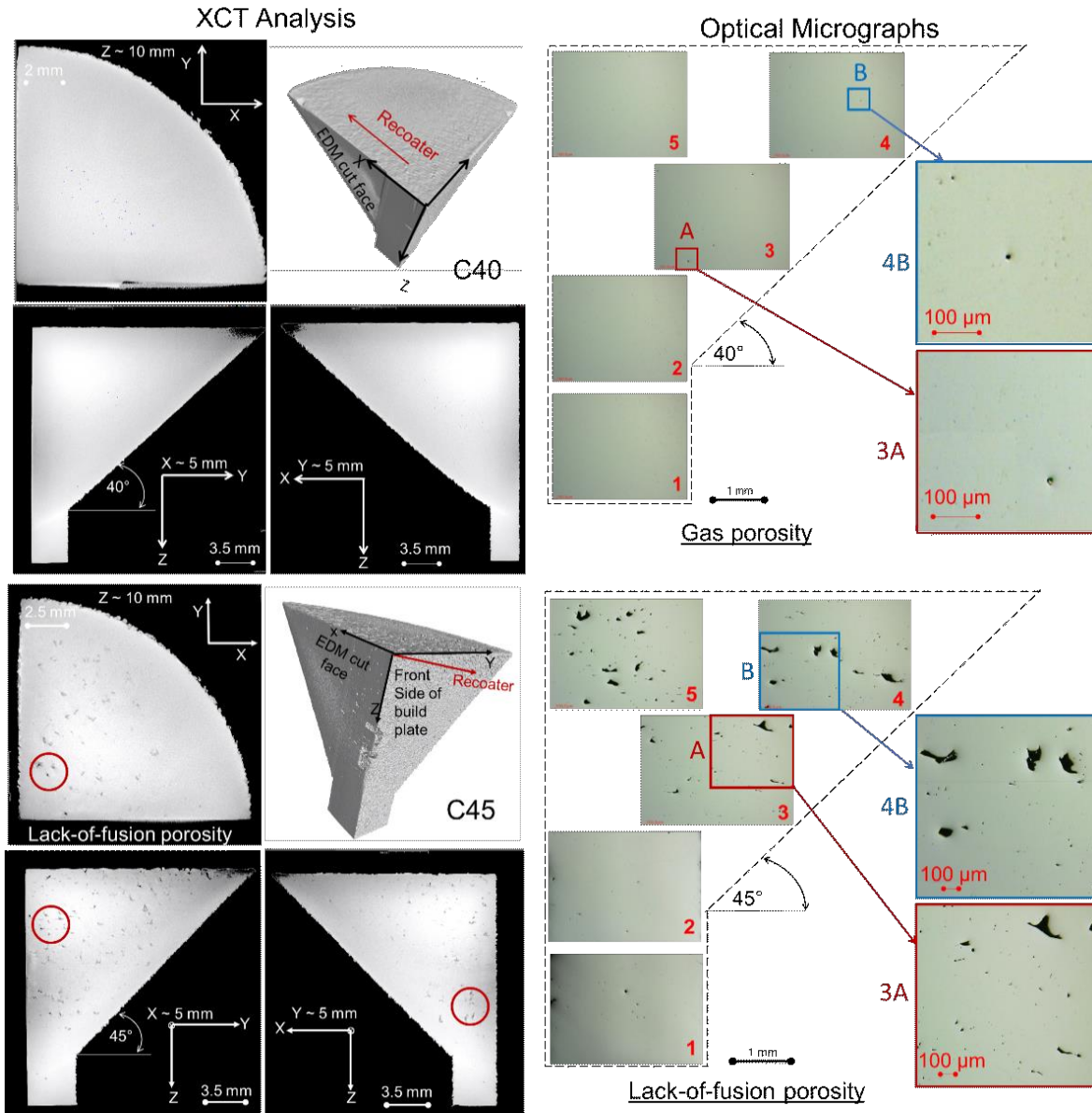


Figure 14: The XCT analysis followed by destructive cross-sectioning for optical imaging of the cone-shaped part reveals the nature of porosity. In C40 (top panel) gas porosity is observed. These pores are likely due to vaporization of gas trapped in the meltpool. In contrast, the test part C45 is replete with irregular shaped pores characteristic of lack-of-fusion.

Table 4: Pore characteristics and percentage porosity for the two cone-shaped parts.

Part	Total Volume of Pores [ $\text{mm}^3$ ]	Total Volume of Part [ $\text{mm}^3$ ]	Porosity [%]
C40	0.36	2517	~ 0.015
C45	25	2036	~ 1.3

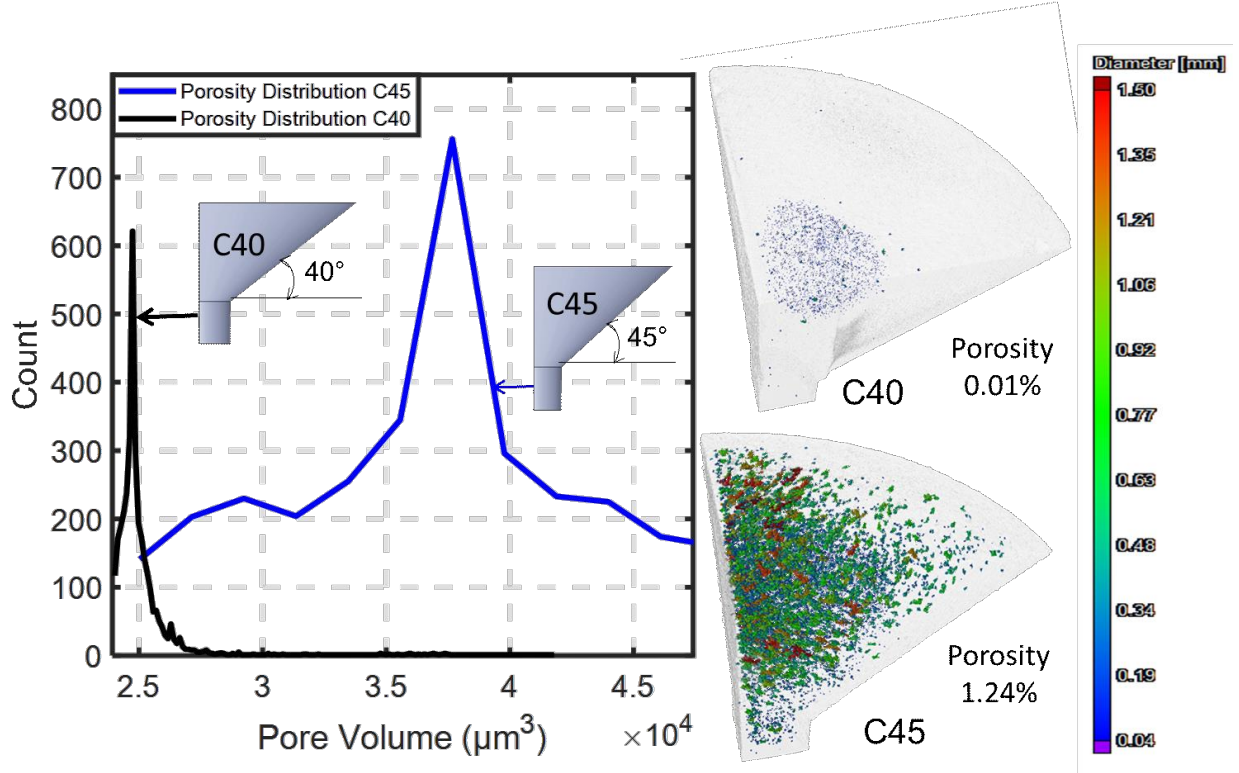
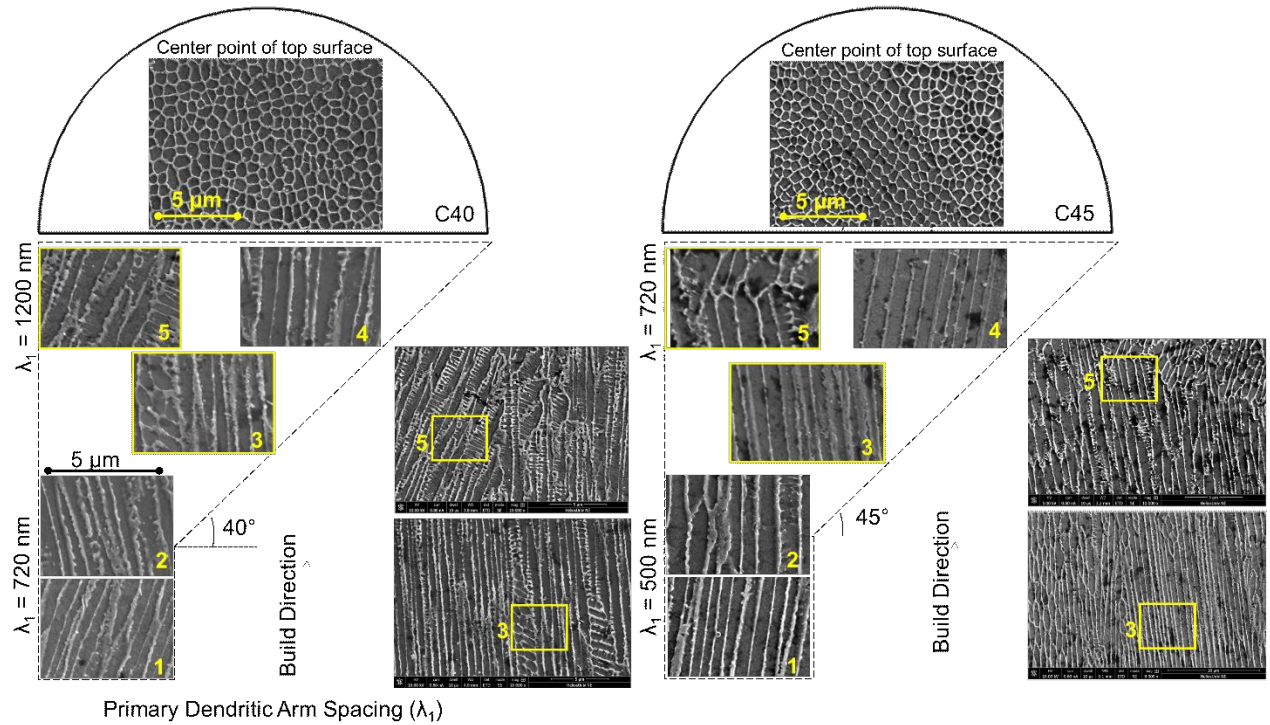


Figure 15: The volume of porosity for the two cone-shaped parts is significantly different. The pores for the cone-shaped part C40 have a significantly smaller size distribution compared to C45. Shown also the XCT images with pore locations mapped in different hues depending on their size.

#### 4.1.3 Microstructure

Figure 16 shows the scanning electron micrographs (SEM) of the XY, YZ and XZ cross-sectional views of the microstructure evolution for the cone-shaped parts. The microstructure evolved consists of columnar and cellular dendrites, as typically observed and reported in simulation and experimental studies in LPBF [80, 82-84]. In LPBF, the dendrites are oriented parallel to the build direction and grow in the direction opposite to the heat flux. The microstructure becomes coarser and the spacing between the dendrites (dendrite arm spacing) increases with the build height. Referring to the cone-shaped part with 40° overhang (C40), the average primary dendrite arm spacing ( $\lambda_1$ ) near the bottom was  $\sim 720$  nm and increased to  $\sim 1200$  nm nearer to the top. In contrast, with the cone-shaped part having 45° overhang (C45) the dendrite arm spacing was  $\sim 500$  nm close to the build plate and only increased to 720 nm nearer the top.

The increase in dendrite arm spacing ( $\lambda_1$ ) with the build height is indicative of heat accumulation, and is in agreement with Figure 13 – the surface temperature increases with the build height [83]. The dendrites are observed to be closer and longer near the build plate due to rapid conduction of the heat into the build plate (heat sink). The larger difference in the dendrite arm spacing ( $\lambda_1$ ) observed for C40 compared to C45 corresponds to the difference in the magnitude of thermal profile observed for the two cones.



*Figure 16: The SEM images of the cone-shaped parts. Both the cone shaped parts, C40 and C45, depict dendrite-type microstructure. The dendrite arm spacing ( $\lambda_1$ ) measured from the SEM images increases with the build height (20 mm) due to the accumulation of heat, and reduction of the cooling rate. There is a distinctive difference in the dendrite arm spacing between the two cone-shaped parts, with C45 showing an overall finer microstructure (i.e., smaller  $\lambda_1$ ) compared to C40, given its more gradual temperature increase.*

To further explain the effect of part geometry on the microstructure for C40 and C45, we analyzed the cooling rate characteristics ( $^{\circ}\text{C}\cdot\text{s}^{-1}$ ) for the surface temperature to cool from the peak melting temperature  $T_0 = 1400^{\circ}\text{C}$  (1673 K) to  $560^{\circ}\text{C}$  ( $\sim 50\%$  of melting temperature  $1673\text{ K} = 836.5\text{ K}$ ) which is shown in Figure 17. The effect of cooling rate on dendritic arm spacing is elucidated by Debroy and co-workers in [1, 83]. The grain morphology and size are functions of the Temperature gradient (G) and growth rate (R). As the cooling rate decreases ( $G \times R$  decreases), the grain size becomes larger [1].

Taken together, Figure 13 and Figure 17 reveal that the cone shaped part C40 tends to retain heat compared to C45. Not only does the surface temperature of C40 increase at a steeper rate compared to C45, but also C40 cools slower than C45 (smaller cooling rate). As a consequence of its slower cooling rate and heat retention, the microstructure for C40 was coarser relative to C45, and which is reflected in the larger primary dendrite arm spacing.

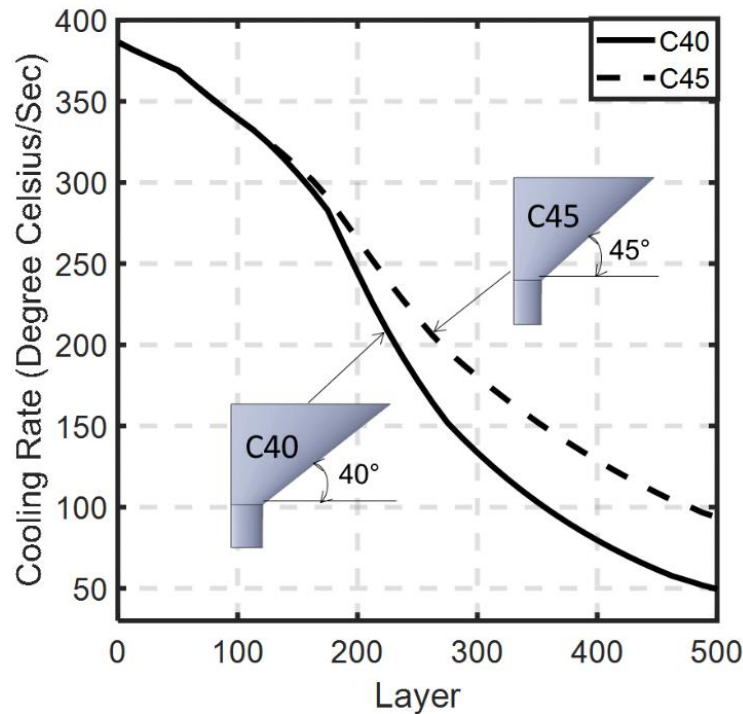


Figure 17. The cooling rate ( $^{\circ}\text{C}\cdot\text{s}^{-1}$ ) taken for the cone-shaped parts to cool from the melting temperature of  $1400^{\circ}\text{C}$  to  $560^{\circ}\text{C}$  (50% of the absolute melting temperature of 1673 K). The cone-shaped part C40 has a slower cooling rate compared to C45, resulting in coarser microstructure.

## 4.2 N-shaped Part

The N-shaped part was used for verifying the graph theory approach in terms of a relatively complex part geometry. As shown in Figure 18, the graph theory approach predictions closely track the surface temperature measurements, until the juncture of the recoater crash, caused by the arch-shaped parts. The MAPE is close to 4% (0.2% standard deviation over 10 iterations), and the RMSE is 9.5 °C (0.8 °C standard deviation). The simulation converged in about 161 seconds.

As discussed previously, clearing a recoater crash is a manual, time consuming process. Consequently, the actual inter-layer time (experimental ILT) deviates from the inter-layer time programed in the G-code (theoretical ILT) – the stoppage caused by the recoater crash causes an increase in the ILT beyond the time allocated in the G-code. In other words, the delay caused by the recoater crash will allow the part to cool for a longer time than programed. Since the model predictions are made using the ILT from the G-code, (i.e., theoretical ILT), there is a deviation in the predicted and experimentally observed surface temperature after the recoater crash.

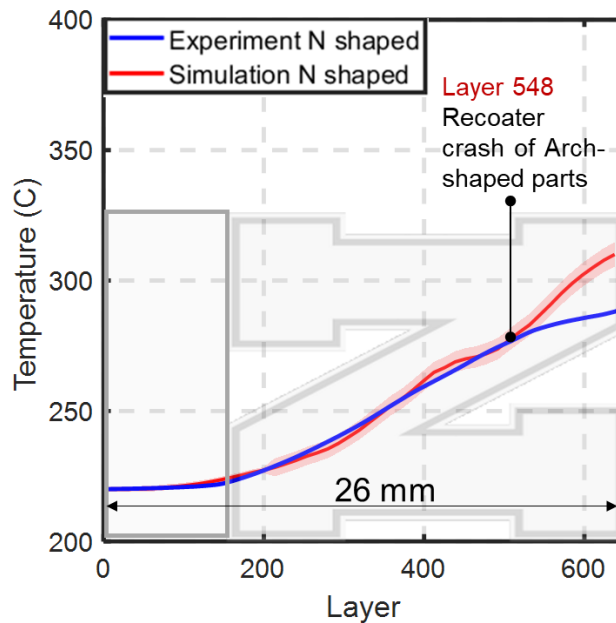


Figure 18: There is a close match in the experimental surface temperature measurements and graph theory predicted temperature trends for the N-shaped part until the point of the recoater crash caused by the arch-shaped parts.

### 4.3 Overhang Parts O45 and O55

#### 4.3.1 Model Performance

In Figure 19, the end-of-cycle surface temperature ( $t_s$ ) distribution predicted for the two overhang parts O45 and O55 is overlaid on the observed surface temperature. The simulation converged in less than 6 minutes; the simulation parameters remain unchanged from the ones calibrated with C45. The convergence behavior is shown in Table 5. As in the cone-shaped parts, the geometry with a shallower overhang tended to have a higher surface temperature distribution. In this case O45, which was inclined at  $45^\circ$  to the horizontal, compared to O55 (inclined at  $55^\circ$  to the horizontal) was predicted to have a higher surface temperature. The surface temperature of the overhang was not as high as for the cone-shaped parts since they have a base with a large cross-section, which acts as a heat sink.

The predicted surface temperature matched the observed surface temperature until layer number 548 (~22 mm build height), where the first of the three recoater crashes occurred concerning the arch-shaped parts. The recoater crash takes close to 15 minutes to clear, and hence the observed surface temperature reduced after layer 548. The mean percentage absolute error was less than 5.5%, with root mean squared error (~12 °C). Until the point of the recoater crash, the observed surface temperature readings are within  $\pm 1$  standard deviation (over 10 replications) of the simulation.

*Table 5. The convergence characteristics for the two overhang parts O45 and O55. The numbers in the parenthesis is the standard deviation over 10 simulation runs.*

Part	MAPE - Before the First Crash (Layer 548) [%]	RMSE- Before the First Crash [°C]	Computation Time (Seconds)
O45	5.4 (0.2)	12.3 (1.8)	336
O55	5.2 (0.3)	11.6 (1.4)	320



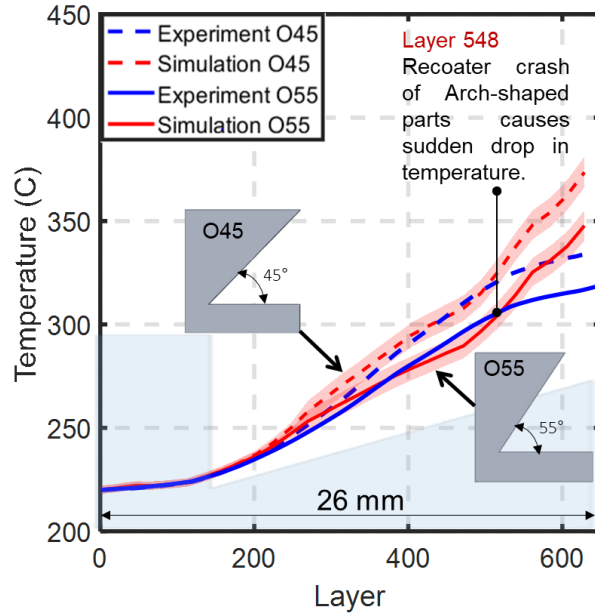


Figure 19: The temperature distribution as a function of the layer numbers for the two prismatic overhang parts O45 and O55. The parts are completed in 650 layers. The part O45 has a steeper temperature profile owing to its increased surface area and volume. The red line in the figure is the predicted temperature with  $\pm 1$  standard deviation, and the blue line represents the observed temperature at the sampled point obtained from the thermal camera.

#### 4.3.2 Porosity Analysis

The porosity resulting from the change in the overhang angle for O45 and O55 is shown in Figure 20 in the context of XCT and optical micrographs. Unlike the cone-shaped parts shown in Figure 14, both O45 and O55 showed lack-of-fusion porosity evident from the irregular-shaped voids. We quantify the pore volume distribution in Table 6 and Figure 21.

The porosity for the part with the shallower overhang (O45) was 0.88%, which is significantly less than for O55 (~1.94%). The exacerbated porosity for the part with the larger overhang angle (O55) is consistent with the results for the cone-shaped parts. Shown previously in Figure 19, the increased surface distribution for O45 is advantageous as it heals the lack-of-fusion pores.

Table 6: Pore characteristics and percentage porosity for the two overhang-shaped parts.

Part	Total Volume of Pores [mm <sup>3</sup> ]	Total Volume of Part [mm <sup>3</sup> ]	Porosity [%]
O45	39	4470	< 0.9
O55	73	3693	< 2%

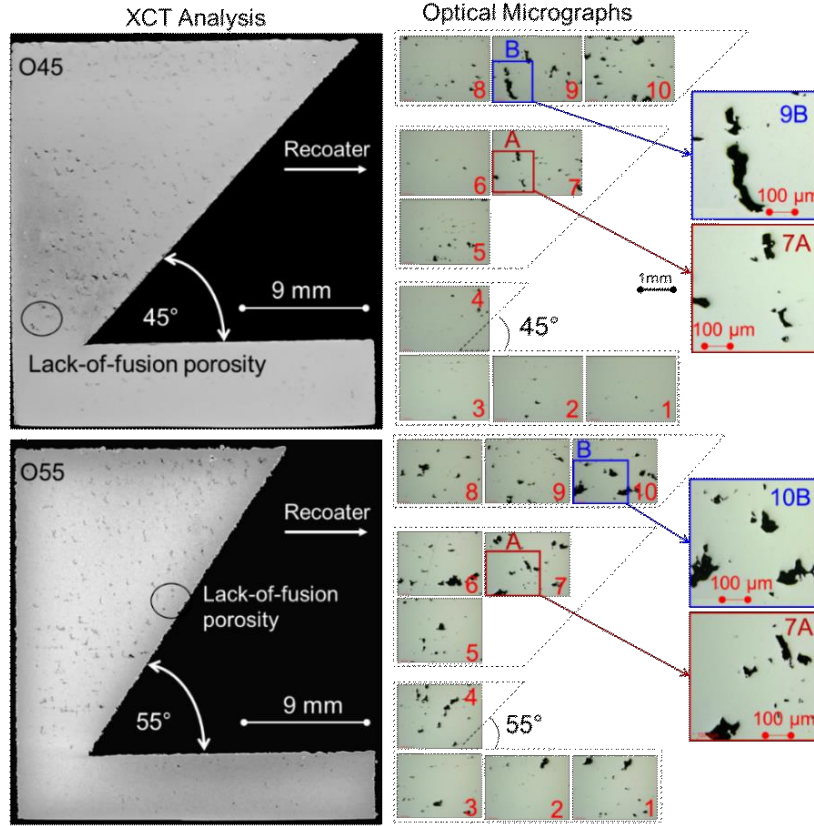


Figure 20: The effect of the overhang angle on porosity formation in the prismatic overhang parts O45 and O55 is evident from the XCT analysis and optical metallographs. While both parts show lack-of-fusion porosity, the severity of pore formation is exacerbated in the overhang part O55.

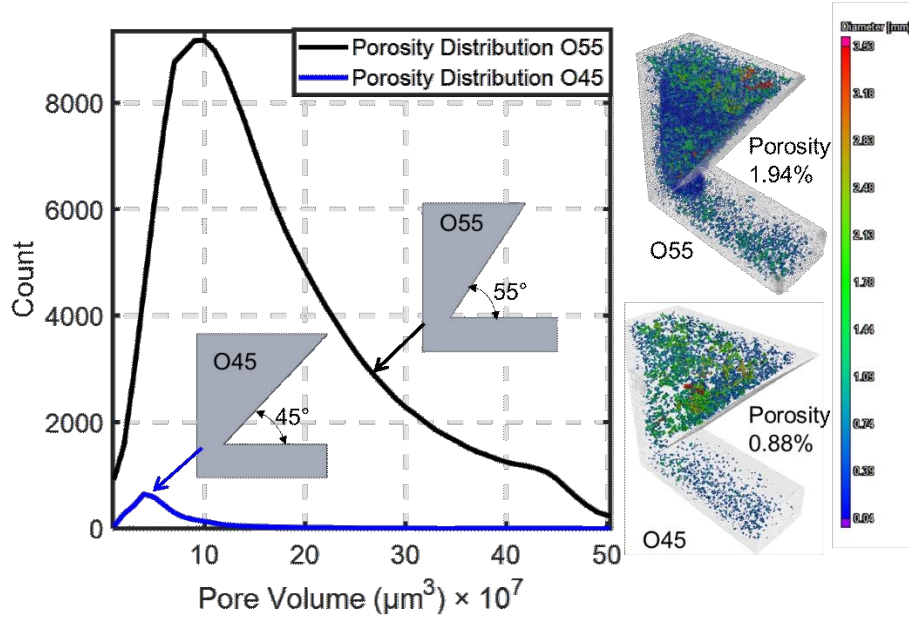


Figure 21: The number of pores for the two prismatic overhang-shaped parts is significantly different. The part with the overhang O45 has a fewer number of pores of a particular size compared to the pores observed in O55. The 3D XCT image is shown in the inset.



#### 4.3.3 *Microstructure*

Shown in Figure 22 are the scanning electron micrographs for O45 and O55. Referring to the micrographs in the X-Z plane, the spacing between the dendrite structures (dendrite arm spacing,  $\lambda_1$ ) for O45 increased from  $\sim 600$  nm from the bottom of the build plate to 900 nm at the top of the part. A similar trend was observed for O55 where the size of dendrite structures increased from approximately 600 nm to 830 nm near the top.

The gradual increase in the size of the dendrites, is attributed to the accumulation of heat and the concomitant decrease in cooling rate with progressive deposition of layers. This result is consistent from previous observation in the context of the cone-shaped part (Figure 16). Hence, the microstructure evolution is not only a function of the build height but also a function of geometry.

Figure 22 also shows SEM images of the XY-plane of O45 and O55 at three different heights. It is observed that the average dendrite core diameter ( $d$ ) was in the range of 720 - 1000 nm and it was slightly larger for O45, except near the very top section. This is because the top section experiences accelerated cooling due to forced convection from the process gases compared to the rest of the part. Moreover, the overhang parts O45 and O55 had considerable high porosity, which can potentially cause anomalous heat flux and thereby lead to swelling of the dendrite cores.

Comparing the microstructure of the overhang shaped part with the cone-shaped parts (Figure 22 vs. Figure 16), the difference in the primary dendrite arm spacing between O45 and O55 is relatively smaller compared to C40 and C45, because, the temperature difference between O45 and O55 is smaller and the temperature rise for the overhang parts was more gradual than for cone-shaped parts. Moreover, three recoater crashes occur between the end of the cone-shaped parts at 20 mm build height (layer 500) and completion of the overhang parts at 26 mm build height (layer

650). Since, it takes close to 15 minutes to reset the machine after each recoater crash, both the overhang parts have longer time to cool. The longer cooling time negates the tendency to retain heat in overhang part O45. Consequently, the microstructure of O45 and O55 is similar.

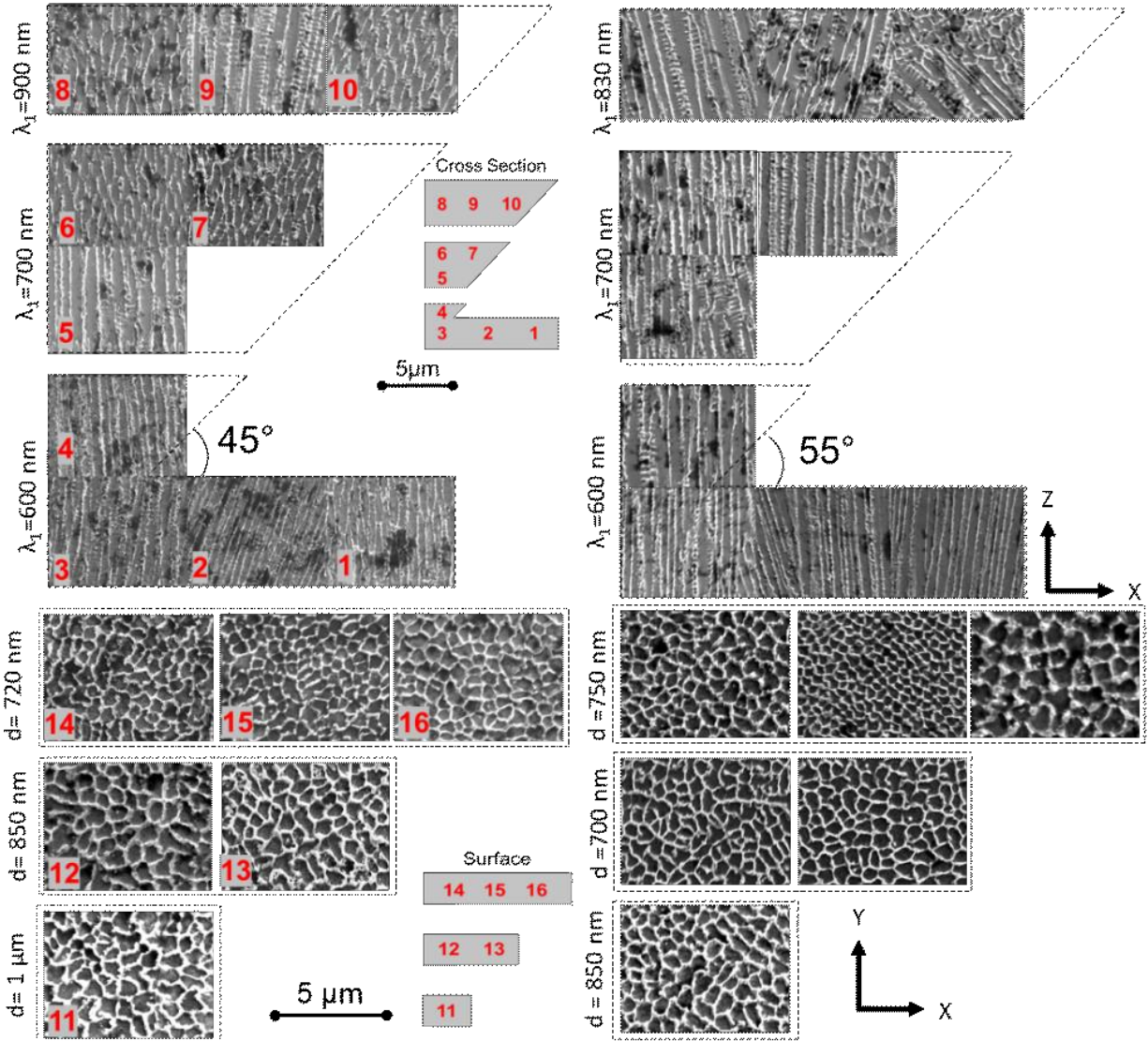


Figure 22. The scanning electron micrographs (SEM) of the overhang parts. Both the overhang shaped parts, O45 and O55, depict dendrite-type microstructure. The primary dendrite arm spacing (PDAS,  $\lambda_1$ ) measured from the SEM images increases with the build height due to the accumulation of heat. The difference in the dendrite arm spacing between the two overhang-shaped parts is not as distinctive as in the cone-shaped parts (Figure 16) as the difference in surface temperature between the two overhang-shaped parts is smaller, and their temperature increase as a function of build height is more gradual. Furthermore, the recoater crash in layer 548 leads to a change in the cooling rate.

## 4.4 Arches

### 4.4.1 Thermal Images of Recoater Crashes

The thermal camera images corresponding to layers where the recoater contacts the arch-shaped parts without supports are shown in Figure 23. Subsequent to the recoater crash in Layer 548, the arch A10 had a higher relative temperature compared to the rest of the arch-shaped parts on the build plate. This is because, following a recoater crash and breakage of the arch A10, the laser can only scan and melt powder without any solidified part underneath. Since, the unconsolidated metal powder is a relatively poor conductor of heat compared to a solidified part, the powder bed surface of a broken part tends to retain heat.

Heat retention is consistently observed subsequent the crash of arch A05 in layer 556, and A20 and A25 in layer 574. Indeed, the debris from the crash of arch A10 is discerned in the thermal images at layer 574.

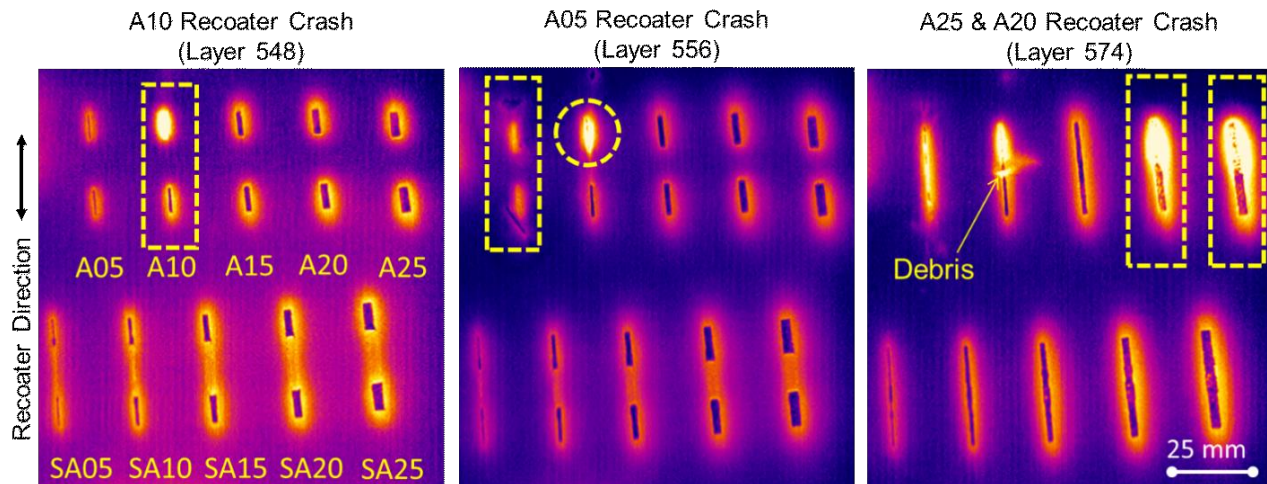
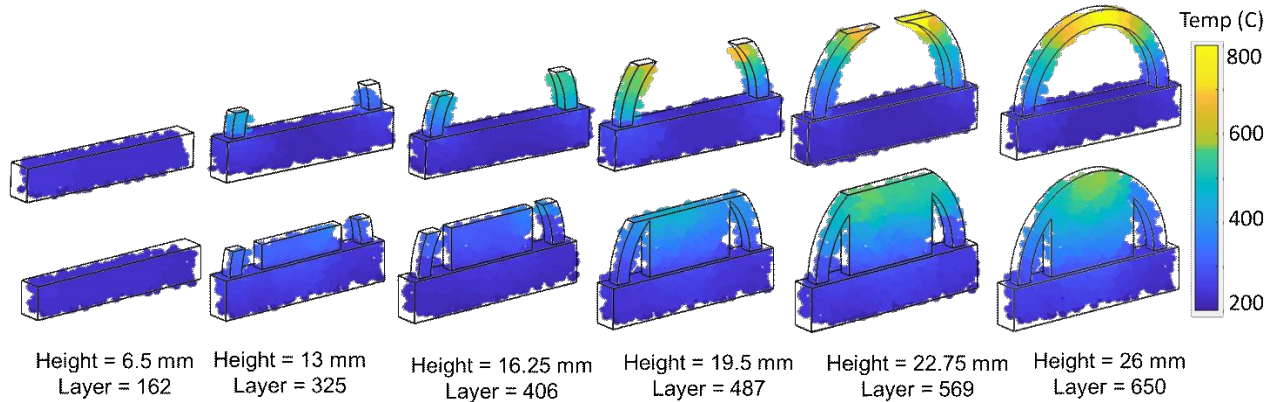


Figure 23: The thermal images obtained from the IR camera for layers 548, 556, and 574 corresponding to recoater crashes caused due to deformation of A10, A05, and A25 and A25. Note the sharp increase in the relative temperature following the failure of the arch-shaped part. The debris from the recoater crash caused by A10 at layer 548 is still evident in Layer 574. Also note the relative difference in the surface temperature between the arches without supports and their counterparts with supports.

#### 4.4.2 Thermal Simulation

The qualitative difference in the layer-by-layer temperature distribution of two types of arches is shown in Figure 24. The arches without supports tended to accumulate heat which led to superelevation (Figure 2), ultimately causing a recoater crash. Since supports conduct heat away from the thin cross-section of the arch, the arches built with supports avoid deformation and subsequent recoater crash.



*Figure 24: The arches built with and without support have significantly different temperature distribution trends. The support structure has the effect of not only providing physical anchoring of the part, but also is a pathway to conduct heat away. In the arches built without support the heat accumulates in the top most portions, while in the part without support the heat is rapidly conducted away.*

In Figure 25, the surface temperature, predicted using graph theory, are overlaid on the experimental for the arches observations. These results are reported in Table 7. All the unsupported arches except the one with 1.5 mm thickness, failed to build on account of the recoater crash. The 0.5 mm and 1 mm thick arches, A05 and A10, failed at the layer number (548 and 556) corresponding to the build height (22 mm). The next to fail were the 2 and 2.5 mm arches A20 and A25, which failed at layer 574 corresponding to a build height of 23 mm. None of the arches with supports failed as the supports prevent heat retention. The 1.5 mm thick arch A15 did not collapse due to the following reason: the superelevation of the neighboring arches surrounding A15 lifted the recoater, thus protecting A15.

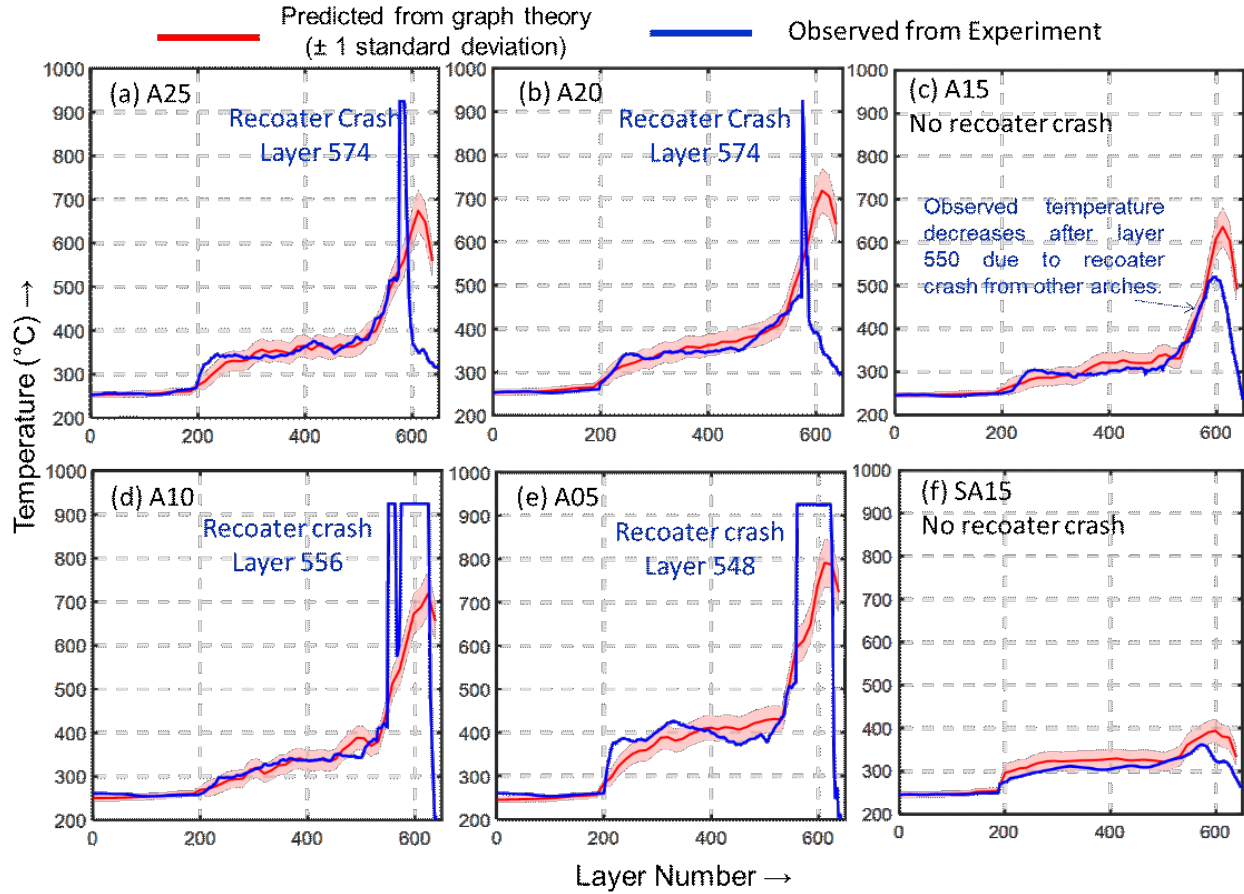


Figure 25: The predicted and observed thermal history for the arch-shaped parts. The temperature trends predicted using the graph theory approach closely match the observed surface temperature until the point of the recoater crash. The thermal history predictions are bounded by  $\pm 1\sigma$  error bounds over 10 replications.

Table 7. Summary of Mean Absolute Percentage Error (MAPE), Root Mean Square Error (RMSE) and computation time for the graph theory simulation of the arch-shaped parts. The numbers in the parenthesis are the standard deviations over 10 replications.

Part	MAPE - before the first crash (Layer 548)	RMSE- before the first crash [°C]	Computation Time [Second]
A25 (Figure 25(a))	4.7 (0.3)	15.4 (1.1)	241
A20 (Figure 25(b))	4.3 (0.3)	13.5 (1.2)	223
A15 (Figure 25(c))	4.9 (0.4)	17.2 (1.4)	214
A10 (Figure 25(d))	4.1 (0.3)	12.5 (1.2)	195
A05 (Figure 25(e))	8.4 (0.5)	31.2 (3.2)	174
SA15 (Figure 25(f))	6.2 (0.4)	24.6 (2.1)	257



This work demonstrates the consequential effect of the thermal history of a LPBF part on the type and severity of porosity, microstructure evolution and process failures (recoater crash). The thermal history of a LPBF part is not only a function of the process parameters, but also influenced by its geometry (shape), placement of supports, and presence of other parts on the build plate. Hence, processing parameters that were optimized based on simple test coupons may not lead to flaw-free parts when used for producing different part shapes or build plans with the same material.

Moreover, a failure in any part on the build plate also affects the thermal history, and thereby the physical properties and microstructure, of other parts on the build plate. For example, a recoater crash will alter the time between layers for the entire build, thus affecting the thermal history. Therefore, to ensure flaw-free production of LPBF parts it is essential to identify and correct red-flag problems in the design and process plan before printing is started through fast and accurate thermal simulation models. Specific findings of this work are as follows:

1. Fifteen different parts encompassing five different shapes (geometries) were built simultaneously on an open architecture LPBF system at Edison Welding Institute. The build time was ~530 minutes (9.5 hours). The thermal history of these parts was predicted using a mesh-free, graph theory approach. Subsequently, these predicted temperature trends were compared with experimental surface temperature measurements obtained using an in-situ infrared thermal camera. The graph theory approach predicted the thermal history for each of the fifteen parts within 5 minutes and root mean squared error less-than 20 °C of experimental temperature observations.
2. Two cone-shaped parts with different overhang angles were studied in this work. The overhang angle ( $Z$ ) is the inclination of the slant edge to the horizontal. The overhang angle has a significant effect on the surface temperature distribution. One of the cone-shaped parts

with  $Z = 40^\circ$  (labeled C40) had a higher temperature compared to the cone-shaped part with  $Z = 45^\circ$  (C45). The pores observed in C45 and C40 are of different types. In C45 irregular-shaped pores characteristic of lack-of-fusion were observed. In C40, the pores were of the gas porosity-type, characterized by their uniform circular shape, most likely due to entrapped gasses escaping from the meltpool. Therefore, the elevated temperature in C40 is advantageous in that it negated the lack-of-fusion porosity observed in C45.

3. The microstructure of the cone-shaped parts was characterized using scanning electron microscopy. Both C45 and C40 depicted dendritic microstructure. The grain size was quantified by measuring the primary dendritic arm spacing ( $\lambda_1$ ). The grains size increased ( $\lambda_1$  increased) in proportion to the part build height due to heat retention and reduction in cooling rate with progressive deposition of layers. The heat retention and reduction in cooling rate is exacerbated for the cone-shaped part with the shallower overhang angle (C40). Consequently, the grain size of C40 is bigger ( $\lambda_1$  is larger) compared to C45. In other words, while C40 has reduced porosity compared to C45, it has a coarser microstructure.
4. Two prismatic parts with overhang angles set at  $Y = 55^\circ$  and  $Y = 45^\circ$  were built (O55 and O45, respectively). Both these overhang parts only showed porosity of one type – lack-of-fusion porosity. As in the cone-shaped parts, the part with the smaller overhang angle  $Y = 45^\circ$ , viz., O45 had a larger surface temperature compared to O55. The overhang part O55 had magnitude greater number of pores than O45. The increased temperature of O45 reduces (heals) the severity of lack-of-fusion porosity observed in O55.
5. The difference in microstructure (grain size) between O45 and O55 was not as prominent as the difference in grain size observed between the two cone-shaped parts. This is likely due to the combined effect of two factors. First, the thermal histories for O45 and O55 are similar.

Second, the cooling time between layers for the overhang parts (O45 and O55) increased on account of three recoater crashes that occur between the completion of the cone-shaped parts at layer 500 and completion of the overhang parts at layer 650.

6. Ten arch-shaped parts were built to test the effect of a continually varying overhang angle, cross-sectional thickness and presence of support structures on thermal history. Four of the five arches without supports failed to build due to recoater crash, while all five arches with supports were completed. The heat retention in arch-shaped parts without supports is significant to cause distortion and subsequent recoater crash. Building arches with supports mitigated the uneven distribution of temperature, and thus avoided failure due to deformation.

This work takes a critical first step for extending the graph theory approach towards understanding and prediction of flaw formation in LPBF. It paves the way to accelerate the time-to-market of LPBF parts by replacing cost- and time-prohibitive empirical trial-and-error testing with a physics-based strategy to tailor the part design, placement of supports and processing parameters. In our future work, we intend to use the graph theory in conjunction with in-process sensor data for process monitoring in LPBF. We are also investigating avenues to combine the graph theory predictions within phase field models to predict occurrence of porosity and microstructural evolution.

### **Acknowledgments**

Prahalada Rao thanks the NSF for funding his research through the following grants CMMI-1719388, CMMI-1739696, CMMI-1752069, and OIA-1929172 at University of Nebraska-Lincoln. Specifically, the concept of using graph theory for modeling in metal additive manufacturing applications is funded through CMMI-1752069 (Program Officer, Dr. Kevin Chou). The NSF grant OIA-1929172 (Program Officer: Dr. Jose Colom-Ustariz) allowed the lead author Mr. Reza Yavari to obtain data at Edison Welding Institute, at Columbus Ohio for validating the graph theory model. Additional supplemental funding for Mr. Yavari was provided through the NSF INTERN program (Program Officer, Dr. Prakash Balan). The authors thank Dr. Jeffrey Shield for insightful suggestions on microstructure characterization.



## Appendix

*The effect of node density and superlayer thickness (SLT) on the mean absolute percentage error (MAPE) and root mean squared error (RMSE). We set SLT = 0.5 mm and node density at 1 node per mm<sup>3</sup>.*

Superlayer Thickness (SLT) [mm] 1 mm = 25 layers	Node Density [Nodes per mm <sup>3</sup> ]	MAPE (%)	RMSE (°C)	Computation Time (sec)
1.5 mm (37.6 layers)	0.2	34.2	29.8	12
	0.6	24.2	21.3	19
	0.8	23.8	20.4	27
	1	21.2	19.5	36
	1.4	17.6	16.2	70
1 mm (25 layers)	0.2	29.6	21.2	13
	0.6	11.0	13.5	27
	0.8	9.3	10.8	38
	1	7.7	8.4	63
	1.4	4.2	6.2	127
0.75 mm (18.75 layers)	0.2	21.1	19.4	13
	0.6	10.6	11.3	26
	0.8	6.9	9.0	45
	1	3.0	5.7	70
	1.4	2.8	5.2	189
0.5 mm (12.5 layers) Selected SLT	0.2	30.5	24.0	14
	0.6	10.3	10.2	36
	0.8	6.6	8.7	68
	1 (selected)	2.7	5.1	113
	1.4	2.3	4.9	283

## References

- [1] DebRoy, T., Wei, H. L., Zuback, J. S., Mukherjee, T., Elmer, J. W., Milewski, J. O., Beese, A. M., Wilson-Heid, A., De, A., and Zhang, W., 2018, "Additive manufacturing of metallic components – Process, structure and properties," *Progress in Materials Science*, 92, pp. 112-224.[doi:https://doi.org/10.1016/j.pmatsci.2017.10.001](https://doi.org/10.1016/j.pmatsci.2017.10.001)
- [2] Sames, W. J., List, F., Pannala, S., Dehoff, R. R., and Babu, S. S., 2016, "The metallurgy and processing science of metal additive manufacturing," *International Materials Reviews*, 61(5), pp. 315-360
- [3] Liu, R., Wang, Z., Sparks, T., Liou, F., and Newkirk, J., 2017, "13 - Aerospace applications of laser additive manufacturing," *Laser Additive Manufacturing*, M. Brandt, ed., Woodhead Publishing, pp. 351-371.
- [4] Dutta, B., and Froes, F. H., 2016, "Chapter 1 - The Additive Manufacturing of Titanium Alloys," *Additive Manufacturing of Titanium Alloys*, B. Dutta, and F. H. Froes, eds., Butterworth-Heinemann, pp. 1-10.
- [5] Dowling, L., Kennedy, J., O'Shaughnessy, S., and Trimble, D., 2020, "A review of critical repeatability and reproducibility issues in powder bed fusion," *Materials & Design*, 186, p. 108346.[doi:https://doi.org/10.1016/j.matdes.2019.108346](https://doi.org/10.1016/j.matdes.2019.108346)
- [6] Snow, Z., Nassar, A. R., and Reutzel, E. W., 2020, "Invited Review Article: Review of the formation and impact of flaws in powder bed fusion additive manufacturing," *Additive Manufacturing*, 36, p. 101457.[doi:https://doi.org/10.1016/j.addma.2020.101457](https://doi.org/10.1016/j.addma.2020.101457)
- [7] Diegel, O., Nordin, A., and Motte, D., 2019, *A Practical Guide to Design for Additive Manufacturing*, Springer, Singapore.
- [8] Mukherjee, T., Manvatkar, V., De, A., and DebRoy, T., 2017, "Mitigation of thermal distortion during additive manufacturing," *Scripta Materialia*, 127, pp. 79-83.[doi:https://doi.org/10.1016/j.scriptamat.2016.09.001](https://doi.org/10.1016/j.scriptamat.2016.09.001)
- [9] Scime, L., and Beuth, J., 2018, "Anomaly detection and classification in a laser powder bed additive manufacturing process using a trained computer vision algorithm," *Additive Manufacturing*, 19, pp. 114-126.[doi:https://doi.org/10.1016/j.addma.2017.11.009](https://doi.org/10.1016/j.addma.2017.11.009)
- [10] Seede, R., Shoukr, D., Zhang, B., Whitt, A., Gibbons, S., Flater, P., Elwany, A., Arroyave, R., and Karaman, I., 2020, "An ultra-high strength martensitic steel fabricated using selective laser melting additive manufacturing: Densification, microstructure, and mechanical properties," *Acta Materialia*, 186, pp. 199-214.[doi:https://doi.org/10.1016/j.actamat.2019.12.037](https://doi.org/10.1016/j.actamat.2019.12.037)
- [11] Gu, D. D., Meiners, W., Wissenbach, K., and Poprawe, R., 2012, "Laser additive manufacturing of metallic components: materials, processes and mechanisms," *International Materials Reviews*, 57(3), pp. 133-164.[doi:10.1179/1743280411Y.00000000014](https://doi.org/10.1179/1743280411Y.00000000014)
- [12] Arisoy, Y. M., Ciales, L. E., Özel, T., Lane, B., Moylan, S., and Donmez, A., 2017, "Influence of scan strategy and process parameters on microstructure and its optimization in additively manufactured nickel alloy 625 via laser powder bed fusion," *The International Journal of Advanced Manufacturing Technology*, 90(5), pp. 1393-1417.[doi:10.1007/s00170-016-9429-z](https://doi.org/10.1007/s00170-016-9429-z)
- [13] Oliveira, J. P., LaLonde, A. D., and Ma, J., 2020, "Processing parameters in laser powder bed fusion metal additive manufacturing," *Materials & Design*, 193, p. 108762.[doi:https://doi.org/10.1016/j.matdes.2020.108762](https://doi.org/10.1016/j.matdes.2020.108762)
- [14] Polonsky, A. T., and Pollock, T. M., 2020, "Closing the science gap in 3D metal printing," *Science*, 368(6491), p. 583.[doi:https://doi.org/10.1126/science.abb4938](https://doi.org/10.1126/science.abb4938)

- [15] Diehl, B., and Nassar, A., 2020, "Reducing near-surface voids in metal (Ti-6Al-4V) powder bed fusion additive manufacturing: the effect of inter-hatch travel time," *Additive Manufacturing*, 36, p. 101592.doi:<https://doi.org/10.1016/j.addma.2020.101592>
- [16] Simpson, T. W., Williams, C. B., and Hripko, M., 2017, "Preparing industry for additive manufacturing and its applications: Summary & recommendations from a National Science Foundation workshop," *Additive Manufacturing*, 13, pp. 166-178.doi:<https://doi.org/10.1016/j.addma.2016.08.002>
- [17] Seifi, M., Salem, A., Beuth, J., Harrysson, O., and Lewandowski, J. J., 2016, "Overview of materials qualification needs for metal additive manufacturing," *Jom*, 68(3), pp. 747-764
- [18] Dovgyy, B., Piglione, A., Hooper, P. A., and Pham, M.-S., 2020, "Comprehensive assessment of the printability of CoNiCrFeMn in Laser Powder Bed Fusion," *Materials & Design*, 194, p. 108845.doi:<https://doi.org/10.1016/j.matdes.2020.108845>
- [19] Ibrahim, Y., Davies, C. M., Maharaj, C., Li, Z., Dear, J. P., and Hooper, P. A., 2020, "Post-yield performance of additive manufactured cellular lattice structures," *Progress in Additive Manufacturing*, 5(2), pp. 211-220.doi:<https://doi.org/10.1007/s40964-020-00128-4>
- [20] Guo, N., and Leu, M. C., 2013, "Additive manufacturing: technology, applications and research needs," *Frontiers of Mechanical Engineering*, 8(3), pp. 215-243.doi:[10.1007/s11465-013-0248-8](https://doi.org/10.1007/s11465-013-0248-8)
- [21] Huang, Y., Leu, M. C., Mazumder, J., and Donmez, A., 2015, "Additive Manufacturing: Current State, Future Potential, Gaps and Needs, and Recommendations," *Transactions of the ASME, Journal of Manufacturing Science and Engineering*, 137(1), p. 014001
- [22] Babu, S. S., Love, L., Dehoff, R., Peter, W., Watkins, T. R., and Pannala, S., 2015, "Additive manufacturing of materials: Opportunities and challenges," *MRS Bulletin*, 40(12), pp. 1154-1161.doi:<https://doi.org/10.1557/mrs.2015.234>
- [23] Oliveira, J. P., Santos, T. G., and Miranda, R. M., 2020, "Revisiting fundamental welding concepts to improve additive manufacturing: From theory to practice," *Progress in Materials Science*, 107, p. 100590.doi:<https://doi.org/10.1016/j.pmatsci.2019.100590>
- [24] Knapp, G. L., Mukherjee, T., Zuback, J. S., Wei, H. L., Palmer, T. A., De, A., and DebRoy, T., 2017, "Building blocks for a digital twin of additive manufacturing," *Acta Materialia*, 135, pp. 390-399.doi:<https://doi.org/10.1016/j.actamat.2017.06.039>
- [25] Martukanitz, R., Michaleris, P., Palmer, T., DebRoy, T., Liu, Z.-K., Otis, R., Heo, T. W., and Chen, L.-Q., 2014, "Toward an integrated computational system for describing the additive manufacturing process for metallic materials," *Additive Manufacturing*, 1-4, pp. 52-63.doi:<https://doi.org/10.1016/j.addma.2014.09.002>
- [26] Mukherjee, T., and DebRoy, T., 2019, "A digital twin for rapid qualification of 3D printed metallic components," *Applied Materials Today*, 14, pp. 59-65.doi:<https://doi.org/10.1016/j.apmt.2018.11.003>
- [27] Thomas, D., 2009, "The development of design rules for selective laser melting," Ph.D. Dissertation, University of Wales.
- [28] Strano, G., Hao, L., Everson, R., and Evans, K., 2013, "A new approach to the design and optimisation of support structures in additive manufacturing," *The International Journal of Advanced Manufacturing Technology*, 66(9-12), pp. 1247-1254
- [29] Peralta, A. D., Enright, M., Megahed, M., Gong, J., Roybal, M., and Craig, J., 2016, "Towards rapid qualification of powder-bed laser additively manufactured parts," *Integrating Materials and Manufacturing Innovation*, 5(1), p. 8.doi:[10.1186/s40192-016-0052-5](https://doi.org/10.1186/s40192-016-0052-5)

- [30] Jared, B. H., Aguilo, M. A., Beghini, L. L., Boyce, B. L., Clark, B. W., Cook, A., Kaehr, B. J., and Robbins, J., 2017, "Additive manufacturing: Toward holistic design," *Scripta Materialia*, 135, pp. 141-147.doi:<https://doi.org/10.1016/j.scriptamat.2017.02.029>
- [31] Druzgalski, C. L., Ashby, A., Guss, G., King, W. E., Roehling, T. T., and Matthews, M. J., 2020, "Process optimization of complex geometries using feed forward control for laser powder bed fusion additive manufacturing," *Additive Manufacturing*, 34, p. 101169.doi:<https://doi.org/10.1016/j.addma.2020.101169>
- [32] Martin, A. A., Calt, N. P., Khairallah, S. A., Wang, J., Depond, P. J., Fong, A. Y., Thampy, V., Guss, G. M., Kiss, A. M., Stone, K. H., Tassone, C. J., Nelson Weker, J., Toney, M. F., van Buuren, T., and Matthews, M. J., 2019, "Dynamics of pore formation during laser powder bed fusion additive manufacturing," *Nature Communications*, 10(1), p. 1987.doi:[10.1038/s41467-019-10009-2](https://doi.org/10.1038/s41467-019-10009-2)
- [33] Gaikwad, A., Yavari, R., Montazeri, M., Cole, K., Bian, L., and Rao, P., 2020, "Toward the digital twin of additive manufacturing: Integrating thermal simulations, sensing, and analytics to detect process faults," *IISE Transactions*, 52(11), pp. 1204-1217.doi:[10.1080/24725854.2019.1701753](https://doi.org/10.1080/24725854.2019.1701753)
- [34] Schoinochoritis, B., Chantzis, D., and Salonitis, K., 2015, "Simulation of metallic powder bed additive manufacturing processes with the finite element method: A critical review," *Proceedings of the Institution of Mechanical Engineers, Part B: Journal of Engineering Manufacture*, 231(1), pp. 96-117.doi:[10.1177/0954405414567522](https://doi.org/10.1177/0954405414567522)
- [35] Bandyopadhyay, A., and Traxel, K. D., 2018, "Invited review article: Metal-additive manufacturing—Modeling strategies for application-optimized designs," *Additive Manufacturing*, 22, pp. 758-774.doi:<https://doi.org/10.1016/j.addma.2018.06.024>
- [36] Olleak, A., and Xi, Z., 2020, "Part-Scale Finite Element Modeling of the Selective Laser Melting Process With Layer-Wise Adaptive Remeshing for Thermal History and Porosity Prediction," *Journal of Manufacturing Science and Engineering*, 142(12).doi:[10.1115/1.4047733](https://doi.org/10.1115/1.4047733)
- [37] Luo, Z., and Zhao, Y., 2018, "A survey of finite element analysis of temperature and thermal stress fields in powder bed fusion Additive Manufacturing," *Additive Manufacturing*, 21, pp. 318-332
- [38] Markl, M., and Körner, C., 2016, "Multiscale Modeling of Powder Bed-Based Additive Manufacturing," *Annual Review of Materials Research*, 46(1), pp. 93-123.doi:[10.1146/annurev-matsci-070115-032158](https://doi.org/10.1146/annurev-matsci-070115-032158)
- [39] Wei, H. L., Mukherjee, T., Zhang, W., Zuback, J. S., Knapp, G. L., De, A., and DebRoy, T., 2020, "Mechanistic models for additive manufacturing of metallic components," *Progress in Materials Science*, p. 100703.doi:<https://doi.org/10.1016/j.pmatsci.2020.100703>
- [40] Dugast, F., Apostolou, P., Fernandez, A., Dong, W., Chen, Q., Strayer, S., Wicker, R., and To, A. C., 2020, "Part-scale thermal process modeling for laser powder bed fusion with matrix-free method and GPU computing," *Additive Manufacturing*, p. 101732.doi:<https://doi.org/10.1016/j.addma.2020.101732>
- [41] Michaleris, P., 2014, "Modeling metal deposition in heat transfer analyses of additive manufacturing processes," *Finite Elements in Analysis and Design*, 86, pp. 51-60.doi:<https://doi.org/10.1016/j.finel.2014.04.003>
- [42] Denlinger, E. R., Gouge, M., Irwin, J., and Michaleris, P., 2017, "Thermomechanical model development and in situ experimental validation of the Laser Powder-Bed Fusion process," *Additive Manufacturing*, 16, pp. 73-80

- [43] Denlinger, E. R., Irwin, J., and Michaleris, P., 2014, "Thermomechanical modeling of additive manufacturing large parts," *Transactions of the ASME, Journal of Manufacturing Science and Engineering*, 136(6), p. 061007
- [44] Pal, D., Patil, N., Zeng, K., and Stucker, B., 2014, "An Integrated Approach to Additive Manufacturing Simulations Using Physics Based, Coupled Multiscale Process Modeling," *Journal of Manufacturing Science and Engineering*, 136(6), pp. 061022-061022-061016.doi:<https://doi.org/10.1115/1.4028580>
- [45] Peter, N., Pitts, Z., Thompson, S., and Saharan, A., 2020, "Benchmarking build simulation software for laser powder bed fusion of metals," *Additive Manufacturing*, 36, p. 101531.doi:<https://doi.org/10.1016/j.addma.2020.101531>
- [46] Zeng, K., Pal, D., Gong, H. J., Patil, N., and Stucker, B., 2015, "Comparison of 3DSIM thermal modelling of selective laser melting using new dynamic meshing method to ANSYS," *Materials Science and Technology*, 31(8), pp. 945-956.doi:<https://doi.org/10.1179/1743284714Y.00000000703>
- [47] Cole, K. D., Yavari, M. R., and Rao, P. K., 2020, "Computational heat transfer with spectral graph theory: Quantitative verification," *International Journal of Thermal Sciences*, 153, p. 106383.doi:<https://doi.org/10.1016/j.ijthermalsci.2020.106383>
- [48] Yavari, M. R., Cole, K., and Rao, P., 2019, "Thermal Modeling in Metal Additive Manufacturing using Graph Theory," *ASME Transactions, Journal of Manufacturing Science and Engineering*, 141(7), pp. 071007-071027.doi:[10.1115/1.4043648](https://doi.org/10.1115/1.4043648)
- [49] Yavari, R., Williams, R. J., Cole, K. D., Hooper, P. A., and Rao, P., 2020, "Thermal Modeling in Metal Additive Manufacturing Using Graph Theory: Experimental Validation With Laser Powder Bed Fusion Using In Situ Infrared Thermography Data," *Journal of Manufacturing Science and Engineering*, 142(12).doi:[10.1115/1.4047619](https://doi.org/10.1115/1.4047619)
- [50] Dunbar, A. J., Denlinger, E. R., Heigel, J., Michaleris, P., Guerrier, P., Martukanitz, R., and Simpson, T. W., 2016, "Development of experimental method for in situ distortion and temperature measurements during the laser powder bed fusion additive manufacturing process," *Additive Manufacturing*, 12, pp. 25-30.doi:<https://doi.org/10.1016/j.addma.2016.04.007>
- [51] Wood, N., Mendoza, H., Boulware, P., and J., H. D., 2019, "Interrogation of mid-build internal temperature distributions within parts being manufactured via the powder bed fusion process," *30th Solid Freeform Fabrication Conference*, Austin, TX., pp. 1445-1481
- [52] Promoppatum, P., Yao, S.-C., Pistorius, P. C., Rollett, A. D., Coutts, P. J., Lia, F., and Martukanitz, R., 2018, "Numerical modeling and experimental validation of thermal history and microstructure for additive manufacturing of an Inconel 718 product," *Progress in Additive Manufacturing*, 3(1), pp. 15-32.doi:[10.1007/s40964-018-0039-1](https://doi.org/10.1007/s40964-018-0039-1)
- [53] Montazeri, M., Yavari, R., Rao, P., and Boulware, P., 2018, "In-Process Monitoring of Material Cross-Contamination Defects in Laser Powder Bed Fusion," *Journal of Manufacturing Science and Engineering*, 140(11).doi:<https://doi.org/10.1115/1.4040543>
- [54] Yu, W. H., Sing, S. L., Chua, C. K., Kuo, C. N., and Tian, X. L., 2019, "Particle-reinforced metal matrix nanocomposites fabricated by selective laser melting: A state of the art review," *Progress in Materials Science*, 104, pp. 330-379.doi:<https://doi.org/10.1016/j.pmatsci.2019.04.006>
- [55] Tenbrock, C., Kelliger, T., Praetzs, N., Ronge, M., Jauer, L., and Schleifenbaum, J. H., 2021, "Effect of laser-plume interaction on part quality in multi-scanner Laser Powder Bed Fusion," *Additive Manufacturing*, 38, p. 101810.doi:<https://doi.org/10.1016/j.addma.2020.101810>

- [56] Sing, S. L., and Yeong, W. Y., 2020, "Laser powder bed fusion for metal additive manufacturing: perspectives on recent developments," *Virtual and Physical Prototyping*, 15(3), pp. 359-370.doi:[10.1080/17452759.2020.1779999](https://doi.org/10.1080/17452759.2020.1779999)
- [57] Poncelet, O., Marteleur, M., van der Rest, C., Rigo, O., Adrien, J., Dancette, S., Jacques, P. J., and Simar, A., 2021, "Critical assessment of the impact of process parameters on vertical roughness and hardness of thin walls of AlSi10Mg processed by laser powder bed fusion," *Additive Manufacturing*, 38, p. 101801.doi:<https://doi.org/10.1016/j.addma.2020.101801>
- [58] Kuo, C. N., Chua, C. K., Peng, P. C., Chen, Y. W., Sing, S. L., Huang, S., and Su, Y. L., 2020, "Microstructure evolution and mechanical property response via 3D printing parameter development of Al–Sc alloy," *Virtual and Physical Prototyping*, 15(1), pp. 120-129.doi:[10.1080/17452759.2019.1698967](https://doi.org/10.1080/17452759.2019.1698967)
- [59] Salmi, A., and Atzeni, E., 2020, "Residual stress analysis of thin AlSi10Mg parts produced by Laser Powder Bed Fusion," *Virtual and Physical Prototyping*, 15(1), pp. 49-61.doi:[10.1080/17452759.2019.1650237](https://doi.org/10.1080/17452759.2019.1650237)
- [60] Williams, R. J., Piglione, A., Rønneberg, T., Jones, C., Pham, M.-S., Davies, C. M., and Hooper, P. A., 2019, "In situ thermography for laser powder bed fusion: Effects of layer temperature on porosity, microstructure and mechanical properties," *Additive Manufacturing*, 30, p. 100880.doi:<https://doi.org/10.1016/j.addma.2019.100880>
- [61] Montazeri, M., and Rao, P., 2018, "Sensor-Based Build Condition Monitoring in Laser Powder Bed Fusion Additive Manufacturing Process Using a Spectral Graph Theoretic Approach," *Journal of Manufacturing Science and Engineering*, 140(9).doi:<https://doi.org/10.1115/1.4040264>
- [62] Atzeni, E., and Salmi, A., 2015, "Study on unsupported overhangs of AlSi10Mg parts processed by Direct Metal Laser Sintering (DMLS)," *Journal of Manufacturing Processes*, 20, pp. 500-506.doi:[dx.doi.org/10.1016/j.jmapro.2015.04.004](https://doi.org/10.1016/j.jmapro.2015.04.004)
- [63] Lane, B., Moylan, S., Whintont, E. P., and Ma, L., 2016, "Thermographic measurements of the commercial laser powder bed fusion process at NIST," *Rapid prototyping journal*
- [64] Mani, M., Lane, B. M., Donmez, M. A., Feng, S. C., and Moylan, S. P., 2017, "A review on measurement science needs for real-time control of additive manufacturing metal powder bed fusion processes," *International Journal of Production Research*, 55(5), pp. 1400-1418.doi:[10.1080/00207543.2016.1223378](https://doi.org/10.1080/00207543.2016.1223378)
- [65] Moylan, S., Whintont, E., Lane, B., and Slotwinski, J., 2014, "Infrared thermography for laser-based powder bed fusion additive manufacturing processes," *AIP Conference Proceedings*, 1581(1), pp. 1191-1196.doi:[10.1063/1.4864956](https://doi.org/10.1063/1.4864956)
- [66] Yavari, R., Williams, R., Riensche, A., Hooper, P. A., Cole, K. D., Jacquetmetton, L., Halliday, H., and Rao, P., 2021, "Thermal Modeling in Metal Additive Manufacturing using Graph Theory – Application to Laser Powder Bed Fusion of a Large Volume Impeller," *Additive Manufacturing*
- [67] Rodriguez, E., Mireles, J., Terrazas, C. A., Espalin, D., Perez, M. A., and Wicker, R. B., 2015, "Approximation of absolute surface temperature measurements of powder bed fusion additive manufacturing technology using in situ infrared thermography," *Additive Manufacturing*, 5, pp. 31-39.doi:<https://doi.org/10.1016/j.addma.2014.12.001>
- [68] Gouge, M., and Michaleris, P., 2018, *Thermo-Mechanical Modeling of Additive Manufacturing*, Elsevier, Cambridge, MA.
- [69] Ganeriwala, R., and Zohdi, T. I., 2014, "Multiphysics modeling and simulation of selective laser sintering manufacturing processes," *Procedia CIRP*, 14, pp. 299-304.doi:<https://doi.org/10.1016/j.procir.2014.03.015>

- [70] Ganeriwala, R., and Zohdi, T. I., 2016, "A coupled discrete element-finite difference model of selective laser sintering," *Granular Matter*, 18(2), p. 21.[doi:https://doi.org/10.1007/s10035-016-0626-0](https://doi.org/10.1007/s10035-016-0626-0)
- [71] Peng, H., Ghasri-Khouzani, M., Gong, S., Attardo, R., Ostiguy, P., Gatrell, B. A., Budzinski, J., Tomonto, C., Neidig, J., Shankar, M. R., Billo, R., Go, D. B., and Hoelzle, D., 2018, "Fast prediction of thermal distortion in metal powder bed fusion additive manufacturing: Part 1, a thermal circuit network model," *Additive Manufacturing*, 22, pp. 852-868.[doi:https://doi.org/10.1016/j.addma.2018.05.023](https://doi.org/10.1016/j.addma.2018.05.023)
- [72] Escolano, F., Hancock, E. R., and Lozano, M. A., 2012, "Heat diffusion: Thermodynamic depth complexity of networks," *Physical Review E*, 85(3), p. 036206.[doi:https://doi.org/10.1103/PhysRevE.85.036206](https://doi.org/10.1103/PhysRevE.85.036206)
- [73] Xiao, B., Hancock, E. R., and Wilson, R. C., 2009, "Graph characteristics from the heat kernel trace," *Pattern Recognition*, 42(11), pp. 2589-2606.[doi:https://doi.org/10.1016/j.patcog.2008.12.029](https://doi.org/10.1016/j.patcog.2008.12.029)
- [74] Zhang, F., and Hancock, E. R., 2008, "Graph spectral image smoothing using the heat kernel," *Pattern Recognition*, 41(11), pp. 3328-3342.[doi:https://doi.org/10.1016/j.patcog.2008.05.007](https://doi.org/10.1016/j.patcog.2008.05.007)
- [75] Saito, N., 2013, "Tutorial: Laplacian Eigenfunctions - Foundations and Applications," University of California, Davis, Graduate University for Advanced Studies, National Institute of Fusion Science, Japan.
- [76] Weber, A., 2008, "Analysis of the physical Laplacian and the heat flow on a locally finite graph," arXiv preprint [arXiv:0801.0812](https://arxiv.org/abs/0801.0812)
- [77] Tootooni, M. S., Rao, P. K., Chou, C., and Kong, Z. J., 2018, "A Spectral Graph Theoretic Approach for Monitoring Multivariate Time Series Data From Complex Dynamical Processes," *IEEE Transactions on Automation Science and Engineering*, 15(1), pp. 127-144.[doi:https://doi.org/10.1109/TASE.2016.2598094](https://doi.org/10.1109/TASE.2016.2598094)
- [78] Chung, F. R. K., 1997, *Spectral graph theory*, American Mathematical Society.
- [79] Çengel, Y. A., & Ghajar, A. J., 2011, *Heat and Mass Transfer: Fundamentals & applications.*, New York: McGraw Hill.
- [80] Cooke, S., Ahmadi, K., Willerth, S., and Herring, R., 2020, "Metal additive manufacturing: Technology, metallurgy and modelling," *Journal of Manufacturing Processes*, 57, pp. 978-1003.[doi:https://doi.org/10.1016/j.jmapro.2020.07.025](https://doi.org/10.1016/j.jmapro.2020.07.025)
- [81] Gaikwad, A., Giera, B., Guss, G. M., Forien, J.-B., Matthews, M. J., and Rao, P., 2020, "Heterogeneous sensing and scientific machine learning for quality assurance in laser powder bed fusion – A single-track study," *Additive Manufacturing*, 36, p. 101659.[doi:https://doi.org/10.1016/j.addma.2020.101659](https://doi.org/10.1016/j.addma.2020.101659)
- [82] Radhakrishnan, B., Gorti, S. B., Turner, J. A., Acharya, R., Sharon, J. A., Staroselsky, A., and El-Wardany, T., 2019, "Phase Field Simulations of Microstructure Evolution in IN718 Using a Surrogate Ni–Fe–Nb Alloy during Laser Powder Bed Fusion," *Metals*, 9(1).[doi:10.3390/met9010014](https://doi.org/10.3390/met9010014)
- [83] Mukherjee, T., Wei, H. L., De, A., and DebRoy, T., 2018, "Heat and fluid flow in additive manufacturing – Part II: Powder bed fusion of stainless steel, and titanium, nickel and aluminum base alloys," *Computational Materials Science*, 150, pp. 369-380.[doi:https://doi.org/10.1016/j.commatsci.2018.04.027](https://doi.org/10.1016/j.commatsci.2018.04.027)
- [84] Qin, H., Fallah, V., Dong, Q., Brochu, M., Daymond, M. R., and Gallerneault, M., 2018, "Solidification pattern, microstructure and texture development in Laser Powder Bed Fusion

(LPBF) of Al10SiMg alloy," Materials Characterization, 145, pp. 29-38.doi:<https://doi.org/10.1016/j.matchar.2018.08.025>